Analysis of Dynamic-Contrast-Enhanced MRI using Model-Based Classification Shapes



Alexandru Badalan

Medical Physics Unit
McGill University
Montreal, Quebec
August 15th, 2022

A thesis submitted to McGill University in partial fulfillment of the requirements of the degree of Master of Science in Medical Radiation Physics

©Alexandru Badalan 2022

ACKNOWLEDGEMENTS

I would first like to acknowledge and give my warmest thanks my supervisor Ives

Levesque for giving me the opportunity to join the MRI methods research group and the freedom
to explore various topics throughout this work. His guidance, insight and advice steered me
through all stages of the project.

I would also like to thank my labmates, Jorge Campos, Véronique Fortier, Evan McNnabb, Leslie Unger, Zaki Ahmed, Marc-Antoine Fortin and Thomas Rosin for their advice, warmth and laughter that kept morale high through endless zoom meetings. This gratitude extends to the other students, staff and faculty of the medical physics unit who kept my spirits high and motivation high during these strange few years working and taking classes from home.

Lastly, I would be remiss in not mentioning my family, especially my parents for their continued support towards my goals over the years.

ABSTRACT

We propose using a shape based algorithm to identify patterns in Dynamic Contrast Enhanced Magnetic Resonance Imaging (DCE-MRI) to assess tumor perfusion as well as automatically delineate the relevant tumor region for analysis. DCE-MRI allows for the imaging of blood perfusion in healthy tissue and in tumours. Previous work has shown that the change in the washout rate of the contrast agent in the tumour between pre-treatment imaging and after one round of chemotherapy appeared to be related to treatment outcome. The proposed method identifies the presence of pre-defined enhancement curves based on the Tofts-Kety model in DCE MRI data. The weight of each curve in the data is estimated using a non-negative least-squares algorithm. The weights of the curves are then used to predict the treatment outcome of the patient. Shape analysis provided meaningful spatial information about tumor perfusion and the dynamics of time series were captured. The therapeutic response of the patients in breast cancer was predicted, even outperforming the predictions based on established quantitative analysis from a previous study. The outcome was the same using either tumor regions of interest delineated by radiologist or automatically. The proposed analysis of DCE-MRI time series using predefined shapes based on the quantitative Tofts-Kety model can provides maps of perfusion characteristics such as slow and fast perfusion. The selection of pre-defined shapes and the interpretations of the weight maps can be adapted based on the application.

ABRÉGÉ

Nous proposons d'utiliser un algorithme basé sur la forme pour identifier les modèles dans l'imagerie par résonance magnétique dynamique de contraste (DCE-MRI) afin d'évaluer la perfusion tumorale ainsi que de délimiter automatiquement la région tumorale pertinente pour l'analyse. La DCE-IRM permet l'imagerie de la perfusion sanguine dans les tissus sains et dans les tumeurs. Des travaux antérieurs ont montré que le changement du taux de lavage de l'agent de contraste dans la tumeur entre un examen avant le traitement et après un cycle de chimiothérapie semblait être relié au résultat du traitement. La méthode proposée identifie la présence de courbes de rehaussement de contraste prédéfinies basées sur le modèle Tofts-Kety dans les données DCE IRM. Le poids de chaque courbe dans les données est estimé à l'aide d'un algorithme des moindres carrés non négatifs. Les poids des courbes sont ensuite utilisés pour prédire le résultat du traitement du patient. L'analyse de la forme a fourni des informations spatiales importantes sur la perfusion tumorale et la dynamique du rehaussement a été décrite. La réponse thérapeutique des patientes atteintes d'un cancer du sein a été prédite, surpassant même les prédictions basées sur une analyse quantitative établie d'une étude précédente. Le résultat était le même en utilisant soit les régions tumorales d'intérêt délimitées par le radiologue, soit des régions définies automatiquement. L'analyse proposée des séries d'images DCE-MRI utilisant des formes prédéfinies basées sur le modèle quantitatif de Tofts-Kety peut fournir des cartes de caractéristiques de perfusion telles que la perfusion lente et rapide. La sélection de formes prédéfinies et les interprétations des cartes de poids peuvent être adaptées en fonction de l'application.

Table of Contents

ACKNO	OWLEDGEMENTS	ii
ABSTR	RACT	iii
ABRÉC	GÉ	iv
PREF A	ACE AND AUTHOR CONTRIBUTIONS	x
Chapter	r 1: Introduction	
1.1	Context and Motivation	1
1.2	Aim of the Research	2
1.3	Outline	3
Chapter	r 2: Background	
2.1	MRI Physics	4
2.1.		
2.1.	e e	
2.1.	e	
2.1.	.4 T ₂ Relaxation	10
2.1.	.5 T ₁ Relaxation	11
2.1.	.6 Basic Pulse sequences	12
2.1.	ε	
2.1.	.8 Gradient echo signals with short TR	
2.2	Dynamic Contrast Enhanced MRI	16
2.2.	.1 Contrast Agents	16
2.3	Shape Analysis in Dynamic Contrast Enhanced MRI	19
2.3.		19
2.3.	<u>. </u>	
2.3.	•	
2.3.		
2.4		
2.4	Breast Cancer Imaging	
2.4. 2.4.		
2.4.	•	
2	•	
-	r 3: Analysis of Dynamic-Contrast-Enhanced MRI using Model-B	· ·
•		
3.1	Abstract	
3.2	Introduction	
3.3	Theory	35
3.4	Methods	37
3.4.		
3.4.	.2 Experimental	38
3.5	Results	41

3.5.	.1 Simulations	41
3.5.	.2 Experimental	41
3.6	Discussion	47
3.7	Conclusion	50
3.8	Acknowledgments	50
Chapter	r 4: Further Analysis with Additional Shape Types and A	Automatic Tumour Delineation
•••••		51
4.1	Shape Analysis with 3 input shapes	51
4.1.	.1 Introduction	51
4.1.	.2 Methods	52
4.1.	.3 Results	52
4.1.	.4 Discussion	54
4.2	Semi-Automatic Region of Interest Generation	55
4.2.	_	
4.2.		
4.2.	.3 Results	57
4.2.	.4 Discussion	61
Chapter	r 5: Discussion & Conclusion	62
5.1	Discussion	62
5.2	Future Work	63
5.3	Conclusion	64
RFFFR	RENCES	66

List Of Figures

Figure 2-1:An illustration of protons and their net magnetization in a hypothetical sample of pure protons (hydrogen nuclei). Protons would not be found in a pure sample like this in reality
Figure 2-2: Illustration of magnetization vectors and components at equilibrium (left) and sometime after a 90-degree pulse
Figure 2-3: Basic Gradient echo pulse sequence showing the initial excitation from a small flip angle, followed by a gradient that is inversed and the resulting echo that is received, adapted from (17) 14
Figure 2-4: T_I -weighted image of the brain, from a patient with cancer of the brain. White and gray matter have intermediate T_I values which results in an intermediate signal. <i>Cerebral</i> spinal fluid has a long T_I and the lowest signal amplitude
Figure 2-5: T_l -weighted image pre (left) and post (right) injection of the contrast agent. The enhancement of the lesion is apparent in the post contrast image. Data from (20)
Figure 2-6: Proposed classification of shape types from Khalifa <i>et al</i> (24). Type I is characterized by persistent enhancement, type II characterized by an initial enhancement followed by a plateau, and type 3 is characterized by an initial enhancement followed by a washout
Figure 2-7: Visual representation of two compartment model. $Ca(t)$ described the arterial input into compartment 1. Exchange occurs between compartment 1 with concentration $C1(t)$ and compartment 2 with $C2(t)$ via $k12$ and $k21$. Elimination occurs from compartment $C1(t)$ via $k10$
Figure 3-1: Top row: Calculated model curves for the Tofts-Kety model, illustrating the impact of variations in each of the model parameters. Note that for the case of constant k_{ep} , the model shape is essentially constant. Bottom row: Calculated model curves for the Tofts-Kety model for a wide range of k_{ep} values, showing the wide range of shapes that can be produced, from very slow and persistent enhancement (very low k_{ep}) to very fast, sharply declining enhancement (very high k_{ep})
Figure 3-2: Plots of the normalized signal-time curves used in the shape analysis of <i>in vivo</i> breast cancer data. The thicker lines are shapes are calculated using the Tofts (75), Vincensini (17), Furman (15) and Eliat (78) studies with the Parker AIF and $T_1 = 1.81$ ms. The faint lines are patient specific shapes calculated using AIFs and T_1 provided with the dataset. Symbols are included to illustrate the data time-points.
Figure 3-3: Simulation results from fitting single-component Tofts-Kety model curves using two (left column) and three (right column) pre-defined analysis shapes. Top row: the shapes (with associated k_{ep} values). Middle row: weights resulting from the analysis. For a range of input (theoretical) model k_{ep}

values from 0.001 to 1.0 min ⁻¹ the model only ever returns non-zero weights for at most two of the predefined shapes. The weight assigned to a given curve peaks at the k_{ep} value of the curve. Bottom row: fitting residuals. The residuals are lowest at or between the k_{ep} of the pre-defined analysis shapes, suggesting that the minimum and maximum k_{ep} values should cover the expected range of shapes 42
Figure 3-4: Effect of varying the number of reference curves (sources) used in weighted fitting on the analysis for 3, 4, and 5 sources. Shows that for any given input curve from a single k_{ep} value, the analysis method uses at most two pre-defined curves with distinct k_{ep} values in the fit. Simulations were performed with up to 5 curves producing results leading to the same conclusion.
Figure 3-5: Fused weight maps for two-shape (low/high) perfusion analysis. The low perfusion weight is represented by the intensity in the blue channel, while the high perfusion weight is in the green channel. In these data from breast cancer patients (freely available from TCIA (76) there appears to be a pattern of perfusion that reflects response to treatment.
Figure 3-6: The mean values of the weights from the two-component analysis of <i>in vivo</i> data can distinguish between patients depending on their pathological response. The distinction is observed on the low-permeability weight at visit 1 in panel (a) (pre-therapy), and the high permeability weight at visit 2 in panel (b) (after 1 cycle of chemotherapy). The analysis is also quite robust to the choice of T_I value and AIF used in the definition of the analysis shapes, suggesting that the method is quite robust. The area under the ROC curve is 1 for all cases except two: at visit 1, using the Parker AIF to define the shapes. 45
Figure 3-7: Histograms of the R^2 values of individual voxels from shape analysis with k_{ep} parameters from the Eliat model. The patients are separated in to pCR and non-pCR visits 1 and two, as well all visit 1 and all visit 2. Shape analysis done on pCR-visit 2 scans are the only ones that do not have R^2 values centered around 0.9, indicating that the model fit is not as good.
Figure 4-1: Shape analysis with 3 shapes reflecting different types of breast cancer. The mean weights of non-zero voxels for each shape are plotted for each patient at visit 1 (left) and visit 2 (right). The AUROC curve for each shape and visit is plotted below each figure. Each patient's response to neo-adjuvant chemotherapy is labelled as pCR (blue) or non-pCR (orange). Separation of pCR and non-pCR patients occurs in the mean weights for the IDC shape in visit 1 and in the mean weights of the ILC shape for visit 2. This is reflected in AUROC values of 1.
Figure 4-2: Shape analysis with the AIF as a third shape. The mean weights of non-zero voxels for each shape are plotted for each patient at visit 1 (left) and visit 2 (right). Each patient's therapy response is labelled as pCR (blue) or non-pCR (orange). The AUROC curve for each shape and visit is plotted bellow each figure. Separation of pCR and non-pCR patients occurs in the mean weights of high-perfusion shapes for visit 2, and the mean weights for low-perfusion shapes in visit 1. This is reflected in AUROC values of 1. The AIF term was characterized by small weights and appears to separate responders from non-responders at visit 2

Figure 4-3: Pipeline for semiautomated region of interest. A rough contour(yellow) is drawn around the tumour, followed by two component shape analysis. Then the shape analysis is restricted voxels that had an R^2 value above 0.5. The last image shows the final contour o the semi-automatic ROI (yellow) 57
Figure 4-4 The DICE coefficients between the manual contours and the semi-automatic contours based on goodness-of-fit is shown in sub plot A. Patients are separated by visit, and each tumour is plotted by a unique colour that is maintained between visits. The size of the manual and semi-automatic tumour contours is plotted in subplot B. Manual and semiautomatic contours sizes for the same tumours are connected by a black line. The DICE coefficients are high, reflecting good conformity between manual and semi-automatic masks. All semi-automatic masks are smaller than their manually drawn counterparts.
Figure 4-5: Mean weights with semi-automatic(top) ROI and manual(bottom) contoured tumours. The mean weights of non-zero voxels for each shape are plotted for each patient at visit 1 (left) and visit 2 (right). Each patient's therapy response is labelled as pCR (blue) or non-pCR (orange). Separation of pCR and non-pCR patients occurs in the mean weights for low-perfusion shapes in visit 1 and in the mean weights of high-perfusion shapes for visit 2 for both of the contouring techniques. The mean weights are similar to those seen with manual ROI, and the separation of therapy response is still present 60
Figure 4-6: Mean weights with semi-automatic threshold ROI. The threshold used was 70% of the maximum enhancement. The mean weights of non-zero voxels for each shape are plotted for each patient at visit 1 (left) and visit 2 (right). Each patient's therapy response is labelled as pCR (blue) or non-pCR (orange). Separation of pCR and non-pCR patients occurs only in the mean weights of high-perfusion shapes for visit 2.

AUTHOR CONTRIBUTIONS

At the heart of this thesis is a manuscript (Chapter 3):

Alexandru Badalan, Zaki Ahmed, Marc-Antoine Fortin, Thomas Rosin, and Ives R Levesque, "Analysis of Dynamic-Contrast-Enhanced MRI using Model-Based Classification Shapes".

that is in preparation for submission to the journal Magnetic Resonance in Medicine.

As the first author I designed and conducted the experiments and conducted the data analysis and writing of the manuscript. Zaki Ahmed conceived of the method, performed an early demonstration of the application, and reviewed the manuscript. Marc-Antoine Fortin conceived of an earlier version of the automatic tumour delineation approach, provided input to the project, and reviewed the manuscript. Thomas Rosin tested the application of the method to liver metastasis and provided insight and input along the whole process. Ives Levesque supervised the project. As my supervisor, he contributed to the design of the methods and experiments, helped interpret the results, and provided guidance at every step of the process, with reviewing manuscript drafts.

Chapter 1: Introduction

1.1 Context and Motivation

DCE-MRI is an MRI technique that involves a series of T_I -weighted images followed by an intravenous injection of a contrast agent. This contrast agent allows for the visualization of perfusion characteristics *in vivo*. This is valuable in oncology as angiogenesis in tumours often produces leaky blood vessels. These blood vessels lead to an abnormal blood supply that manifests as a rapid enhancement in the DCE-MRI signal compared to healthy tissue (1).

DCE-MRI is often performed with three-dimensional T_I -weighted spoiled gradient echo imaging with a trade-off between spatial and temporal resolution (2). Sufficient temporal resolution is important to capture the passing of the contrast agent through blood vessels and into the surrounding intracellular interstitial space.

Qualitative analysis of DCE-MRI data can include visualization of the individual images by a trained expert or observation of the time-variation in a region of interest, and is a mainstay in the clinical application of this approach (3). For example, averaging the voxels in a region of interest and inspecting at the average signal curve has been successful in characterizing lesions as either benign or malignant in breast (4) and in soft tissue tumours (5). Qualitative analysis is fundamentally subjective, time consuming and requires experience for interpretation.

This has created an interest in employing computational algorithms to introduce a layer of objectivity to the analysis, to develop a potential imaging biomarker that is reproducible and validated, and to speed up the processing time. Semi quantitative methods are straightforward, and can involve computing the maximum enhancement (6), the slope of the initial enhancement (7), or the initial area under the enhancement curve (to a pre-selected time-point) (8). The popular three-time-point method (9) is another form of semi-quantitative analysis, that relies on the signal

change between successive images at specific times (one pre-injection and two post-injection). Semi-quantitative analysis is fast, but inter-patient comparison is difficult as it does not account for variability in the scanner hardware or contrast agent injection protocols.

Methods of quantitative analysis were developed to account for inter-patient and interscanner variability and to provide quantitative parameters that could potentially be connected to biological or physical characteristics. Ideally, a T_1 map would be required at each time-point in the series, but with some manipulation and pre-contrast proton-density-weighted images and T_1 map, the dynamic T_l -weighted signal can be converted to tissue contrast-agent concentration (10). Compartmental models such as the Tofts-Kety (11), extended Tofts-Kety (11), Larsson model (12), Brix model (13), Patlak approach (14), or two compartment exchange model (15) can be applied to extract several physical parameters that have garnered considerable interest in scientific literature. Quantitative DCE-MRI analysis is interesting but can be challenging due to the need for high temporal resolution (and the resulting trade-off with spatial resolution and/or signal-to-noise ratio), the need for a pre-injection T_I map, the challenges associated with determining the dynamics of contrast agent concentration in blood plasma (the so-called arterial input function), model selection, the non-linear nature of model analysis, and the potentially confounded interpretation of the parameters (e.g. the interpretation of K^{Trans} in the flow-limited or permeability limited regime). And so, clinical use has generally favoured qualitative or semi-quantitative analysis, for the simplicity of the analysis, though K^{Trans} mapping has emerged as a clinical tool (3).

1.2 Aim of the Research

A proposed alternative to analyze DCE-MRI data comes in the form of shape analysis. Several groups have proposed to extract characteristic time curves from the DCE data series (3), often known as *sources*, and produce maps of the spatial distribution of the presence of these

sources in the data, known as *weight maps*, effectively representing the DCE data using a small set of data-generated characteristic curves. The source or shape is a trend of signal as a function of time. This can allow for the spatial distribution of perfusion to be viewed as a mixture of these shapes at each voxel.

In this work we exploit an observation by Tofts *et al.* that the parameter k_{ep} is sufficient to describe the unique shapes of time courses seen in tumours (16), to develop a technique to analyze DCE-MRI data. The method uses a small set of predetermined shapes derived from the Tofts-Kety model and identifies their weight within voxels based on a non-negative least-squares analysis. Values of k_{ep} are selected from previous literature reflecting malignant or benign tumours. We developed an easier approach to analysing DCE MRI data that provides meaningful spatial characterization of perfusion. In a key application, results suggest a predictive ability of this approach for the therapeutic outcome of neoadjuvant chemotherapy. Advantages of this method include robustness at low temporal resolution, faster processing speed, and an absence of need for independent T_I mapping.

1.3 Outline

Chapter 2 will cover the background physics required for acquisition and analysis of DCE MRI in greater detail. This will include fundamentals of MRI physics and DCE-MRI, basic notions about MR imaging in breast, and a review of the literature on shape analysis in DCE-MRI. Chapter 3 will contain the main body of the work in the form of a manuscript to be submitted to *Magnetic Resonance in Medicine*. Chapter 4 expands the shape analysis method to 3 source curves and investigates an alternate use of the model to automatically generate regions of interest surrounding tumours. These additional results were produced over the course of the project but were not included in the manuscript for submission, out of concern for brevity and scope. Finally, Chapter 5 will conclude this thesis by discussing applications, future work, and conclusions of this work.

Chapter 2: Background

This chapter will cover the background physics required to understand the acquisition and processing of DCE-MRI data. It will begin by covering the fundamentals of MR physics, followed by the introduction of MR parameters and pulse sequences, including methods to generate T_I and T_2 -weighted images and the role contrast agents can play in these images. This chapter will conclude with an overview of relevant qualitative and quantitative techniques for analysis of contrast enhanced MRI. The clinical role of MRI regarding breast cancer will be introduced next, including the techniques used and some technical requirements

2.1 MRI Physics

The following section is an overview the fundamentals of MR physics based on the information presented in Chapters 12 and 13 from *Jerrold T. Bushberg's The Essential Physics of Medical Imaging* (17) and Chapters 3 and 4 from *Dwight G. Nishimura's Principles of Magnetic Resonance Imaging* (18).

2.1.1 Origin of the MR signal

The origin of the MR signal comes from the magnetic moments of certain atoms. Basic particles including protons, neutrons, and electrons have a quantum mechanical property called "spin". Although the particles are not actually spinning, they have an angular momentum as if they were spinning, thus the name. This angular momentum can result in a non-zero magnetic moment. Atomic nuclei with a sum of neutrons and protons that are not even have a non-zero magnetic moment, characterized by their non-integer nuclear spin (S). Despite this, a single nuclear magnetic moment is not large enough to be experimentally observable, but the combined magnetic moment of a large number ($\sim 10^{15}$) of atoms would be. There are several candidate atoms with magnetic

moments, but to be biologically relevant they must have: a strong nuclear magnetic moment, large physiologic concentration, and large isotope abundance. Candidates of this include: ¹H, ³He, ¹³C, ¹⁷O, ¹⁹F, ²³Na, and ³¹P. Hydrogen meets all these criteria by having the largest nuclear magnetic moment and abundance, thus being the best element for clinical utility and the principal focus for generating MR signals. The nucleus of a hydrogen atom is a proton, and proton and hydrogen will be used interchangeably throughout the rest of this thesis.

2.1.2 The Effect of a Magnetic Field

Classically, the proton can be considered as a small bar magnet. Hydrogen attached to unbound molecules of fat and water have random orientations of their magnetic moments. However, when placed inside a magnetic field of B_0 , the protons' magnetic moments will align themselves either parallel or anti parallel to the B_0 . Nuclear spin is a quantum mechanical property, and protons having a spin of $\frac{1}{2}$ can only exists in two states. Thus, the spins in the parallel direction are in a lower energy state $\left(-\frac{1}{2}\right)$ while the spins in the anti-parallel direction are in a higher energy state $\left(+\frac{1}{2}\right)$. The difference between these two energy states is given by:

$$\Delta E = h \frac{\gamma}{2\pi} B_0$$

(2-1)

Where h is plank's constant (6.62607015 x 10^{-34} m² kg/s), $\frac{\gamma}{2\pi}$ is the gyromagnetic ratio (42.58 MHz/T for hydrogen). The difference between the two energy states is small enough that thermal energy is enough to exceed the separation. This means that despite the tendency toward lower energy states, some spins can still occupy the higher energy state. Under thermal equilibrium there is a slight majority of protons in the parallel direction. This excess can be approximated by:

$$\frac{n_+}{n_-} \approx n_s \frac{\gamma h B_0}{4\pi k_B T}$$

(2-2)

Where n_s is the total number of nuclei spins, n_- is the total number of lower energy spins, n_+ is the total number of higher energy spins, $\frac{\gamma}{2\pi}$ is the gyromagnetic ratio, h is Planck's constant, k_B is Boltzmann constant (1.380649×10⁻²³ m² kg s⁻² K⁻¹), and T is temperature in kelvin. From equation (2-2), it can be seen that the only adjustable variables are temperature T and magnetic field $\mathbf{B_0}$. Since $in\ vivo$ imaging requires a specific temperature to keep the subject comfortable/alive, only $\mathbf{B_0}$ has room to be adjusted. A larger magnetic field increase the ratio $\frac{n_+}{n_-}$, thus increasing the number of spins in the lower state. At 1.0 T the number of excess protons in the low energy state is approximately 3 per million. This may seem like a minuscule amount, but when considered that for a typical MRI scan volume there are about 10^{21} protons, there will be 3×10^{15} more protons in the low energy state. Since each proton has a magnetic moment either aligned in parallel or anti parallel with the field, a net excess of spins in the lower energy state provides the sample with a net magnetic moment \mathbf{M} aligned with $\mathbf{B_0}$.

In the external magnetic field spins also experience a torque in the perpendicular direction. This causes a precession similar to the wobbling of a spinning top and it occurs at an angular frequency proportional to \mathbf{B}_0 known as the Larmor frequency f_0 . This is described by the *Larmor Equation*:

$$f_0 = \frac{\omega_0}{2\pi} = \frac{\gamma}{2\pi} B_0$$

(2-3)

Where γ is the gyromagnetic ratio unique to each element with a non-zero magnetic moment and \mathbf{B}_0 is the static magnetic field. The net magnetic moment of the sample will be equal to the

individual sum of all vector moments. Any perpendicular components of the nuclei are randomly oriented and sum to zero. Briefly irradiating the sample with a radiofrequency (RF) pulse \mathbf{B}_1 tuned to the Larmor frequency "excites" protons from the low energy to the high energy. This is the resonance of magnetic resonance imaging.

This pulse is generated by a radiofrequency coil. Radiofrequency coils are essential components of the MRI system. They are highly sensitive antennas used to either transmit or receive signals. An RF transmit coil (Tx) generates the RF pulse that rotates the net magnetization away from its alignment with the main magnetic field. The receive coil (Rx) detects the precessing magnetization as an electric current induced via electromagnetic induction.

From a classical perspective, the magnetic field of the RF pulse induces a torque on the magnetization **M** to rotate away from its equilibrium position. As the newly promoted samples return from their higher energy state to equilibrium conditions RF energy is released, which is then detected by the receive coils. The interaction of all these elements of protons in a magnetic field is shown in Figure 2-1.

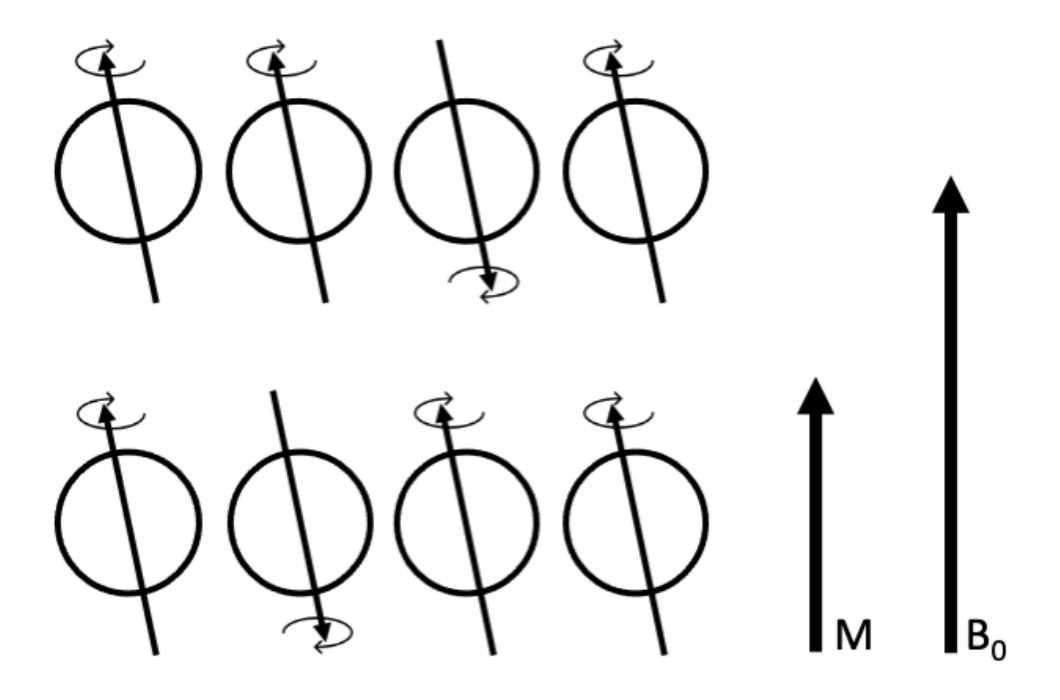


Figure 2-1: An illustration of protons and their net magnetization in a hypothetical sample of pure protons (hydrogen nuclei). Protons would not be found in a pure sample like this in reality.

2.1.3 Resonance

The magnetic field generated by M is difficult to measure since it is much smaller than B_0 . M is a vector in 3D space and can also be broken down into two components: M_{xy} is the transverse magnetization perpendicular to the magnetic field and M_z is the longitudinal magnetization parallel to the magnetic field. At equilibrium, M is maximal and denoted as M_0 . This can be changed by applying a RF pulse B_1 .

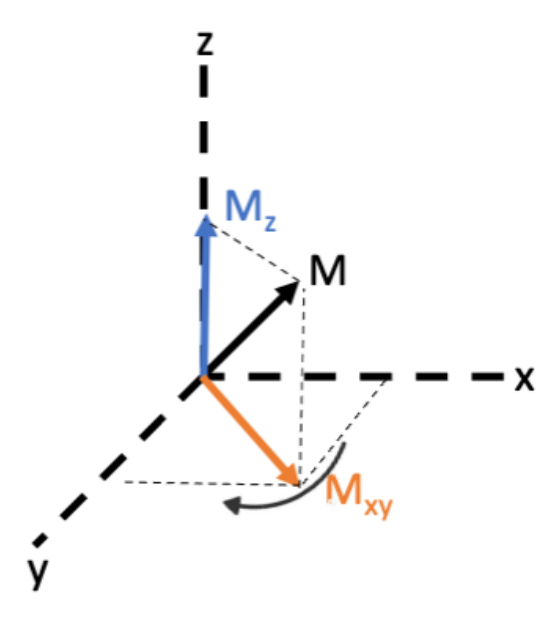


Figure 2-2: Illustration of magnetization vectors and components at equilibrium (left) and sometime after a 90-degree pulse.

MRI physics can be modeled through either a classical or a quantum mechanical point of view. The classical model is sufficient for modeling and will be the focus of this chapter. In the classical physics model the RF pulse is composed of alternating magnetic field. Optimally, the B_1 is described as a single circularly polarized field synchronized with precession. The displacement of the magnetization away from magnetization occurs when the magnetic component of the RF pulse matches the precessional frequency of the protons. B_1 applies a torque on M rotating it from the longitudinal direction onto the transverse plane. The degree of rotation of M is called the flip angle and the rate of rotation is $\omega_1 = \gamma B_1$, as per the Larmor equation. Common flip angles are 90 degrees and 180 degrees. A 90-degree angle provides the largest possible M_{xy} and detectable

MR signal for the initial condition $\mathbf{M}_{\mathbf{z}}(0) = \mathbf{M}_{\theta}$. Such a large flip angle also requires the largest amount of time to displace. Fast MRI sequences use flip angles of 10 or less.

The M_{xy} component of M will start rotating at an angular frequency ω_0 around the Z axis. This rotation of the M_{xy} component induces an electromotive force in the receiver coil by producing a time varying magnetic field. Measuring this force in the receiver coil will produce a signal proportional to the magnitude of M_0 . Acquiring this at different locations will produce an image where contrast is created by the density of protons or M_0 in the sample. Unfortunately, this will result in limited soft tissue contrast in a human body, as the density of protons is mostly uniform across most soft tissue. However, after excitation the protons experience a relaxation that brings their magnetic moment towards equilibrium, and this is exploited to generate additional contrast.

2.1.4 T₂ Relaxation

After a \mathbf{B}_1 pulse, an initial phase coherence of proton magnetization is established resulting in \mathbf{M}_{xy} . Rotating at the Larmor frequency, the transverse magnetic field induces a signal in the receiver coil. This signal is known as free induction decay (FID). A loss in the FID signal is caused by a loss of \mathbf{M}_{xy} phase coherence due to inhomogeneities in the sample. This is caused by individual protons precessing at slightly different frequencies due to microscopic magnetic inhomogeneities in the sample. The loss follows an exponential decay given by

$$\mathbf{M}_{xy}(t) = \mathbf{M}_{xy}(0)e^{-\frac{t}{T^2}}$$
(2-4)

Where $\mathbf{M}_{xy}(t)$ is the transverse magnetic moment at time t for a sample that has $\mathbf{M}_{xy}(0)$ transverse magnetization at t=0. T_2 is the exponential decay constant, or the time over which the signal decays to 37% of the initial transverse magnetization. This decay is strongly affected by the

molecular structure of the sample and characteristics of water bound protons. Small molecules have a large T_2 , and their slow FID is caused by molecular tumbling and diffusion. As molecular size increases, constrained motion and hydration layers will increase spin dephasing, shortening T_2 . Extrinsic field inhomogeneities such as an imperfect magnetic field or susceptibility agents in tissues add to the loss of phase coherence. These effects are not random and can be considered separate from the "pure" T_2 processes, and result in a total transverse relaxation constant given by

$$\frac{1}{T_2^*} = \frac{1}{T_2} + \frac{1}{T_2'}$$

(2-5)

Where T_2^* is the total transverse relaxation constant, T_2^* is the spin dephasing due to random fluctuations and T_2' is the spin dephasing due to static processes.

2.1.5 T₁ Relaxation

Longitudinal relaxation of the magnetization vector begins after the $\mathbf{B_1}$ excitation pulse. It occurs simultaneously to transverse relaxation but over a longer period of time. It also occurs exponentially given by the equation:

$$\mathbf{M}_{z}(t) = \mathbf{M}_{0} + (\mathbf{M}_{z}(0) - \mathbf{M}_{0})e^{-\frac{t}{T_{1}}}$$
(2-6)

Where $\mathbf{M_z}(t)$ is the longitudinal magnetic moment at time t, and T_I is the time needed for the recovery of 63% of its maximum value. However, since the signal is generated by $\mathbf{M_{xy}}$, measuring $\mathbf{M_z}$ requires a particular sequence of events also referred to as a pulse sequence. At equilibrium, a 90-degree pulse sets $\mathbf{M_z}$ to 0. After a delay time of ΔT , $\mathbf{M_z}$ is converted to $\mathbf{M_{xy}}$ by a second 90-degree pulse. The recovered $\mathbf{M_z}$ is now the measurable $\mathbf{M_{xy}}$, and the resulting peak amplitude is recorded. This sequence is repeated with different delay times ΔT to obtain data points on a curve

that is then fitted with equation (2-6) from which T_I can be estimated. T_I relaxation depends on the rate of energy dissipation into the surrounding molecular lattice, strongly dependent on physics characteristics of tissues and hydration layers. T_I values can typically range from 0.1 to 1 s for soft tissues and 1 to 4 s in aqueous tissues. As will be described in section 2.2.1, paramagnetic gadolinium chelated with complex macromolecules is effective in decreasing T_I relaxation time in nearby hydrogen protons in the tissue through the hydration layer that forms around the macromolecule, creating a spin-lattice energy sink and resulting in a rapid return to equilibrium.

2.1.6 Basic Pulse sequences

Generating contrast in MR images can be achieved by exploiting differences between the T_1 and T_2 relaxation time constants and proton density of tissues. MR imaging consist of a series of repeated sequences of magnetic field pulses to build complete data set over time. The time of repetition (TR) is the period between successive $\mathbf{B_1}$ excitation pulses. As described in a previous section, excitation of protons with $\mathbf{B_1}$ pulses results in the creation of an $\mathbf{M_{xy}}$ free induction decay signal. Under static effects (T_2^*) the spin vectors will spread out in the transverse plane. This phase accumulation is proportional to time since the pulse. A 180-degree RF pulse or a gradient echo is used to reverse the polarity of the spins in order to create an "echo" to separate the RF energy deposition and returning signal. Since the spins started out in phase and gradually fell out of phase, the reversing pulse causes the spins to begin returning into phase, matching phase at TE or the "echo". The resulting "spin" echo can be observed. TE is the time between delivery of the RF pulse and the reception of the echo signal. Since the echo is received at TE, the 180-degree RF pulse is delivered at TE/2.

The inversion time (TI) is the time between an initial inversion and the 90-degree readout pulse that converts $\mathbf{M}_{\mathbf{z}}$ to $\mathbf{M}_{\mathbf{x}\mathbf{y}}$. During the inversion time, $\mathbf{M}_{\mathbf{z}}$ regrows in the +z direction as it

returns to equilibrium. If at TI, the M_z happens to be at or near zero at the time of the readout pulse, the M_{xy} will be at or near zero and contribute little to no signal. Since different tissues relax at different rates, their M_z will cross the zero boundary at different times, and TI can be chosen to selectively null particular tissues. On common example is to null the signal from fat tissue.

It is common in MR imaging to desire to suppress the signal from fat in order to better visualize a tissue of interest. Water-fat separation can be done by exploiting either the water-fat resonance frequency difference, the short T_1 of fat or both (19). These can include chemically selective fat suppression pulses, spatial-spectral pulses, short inversion time recovery imaging, chemical shift-based fat separation methods and fat suppression with balanced steady-state free precession. More detail on fat suppression can be found in a review by Bloy *et al* (19).

This section will focus on a pulse sequence technique known as gradient echo (GRE) as it is the most used with DCE MRI. As the name implies GRE techniques use a magnetic field to generate transverse magnetization. The FID manipulated with a field gradient pulse has a transverse magnetization that dephases rapidly as the gradient is applied. The gradient echo generated is used twice in succession. First it is used with a negative polarity to enforce transverse dephasing of spinning protons, and then with a positive polarity to re-align the dephased protons and acquire a signal as shown in Figure 2-3. This sequence is particularly useful for emphasizing magnetic field inhomogeneities caused by paramagnetic tissues, diamagnetic tissues, or contrast agents.

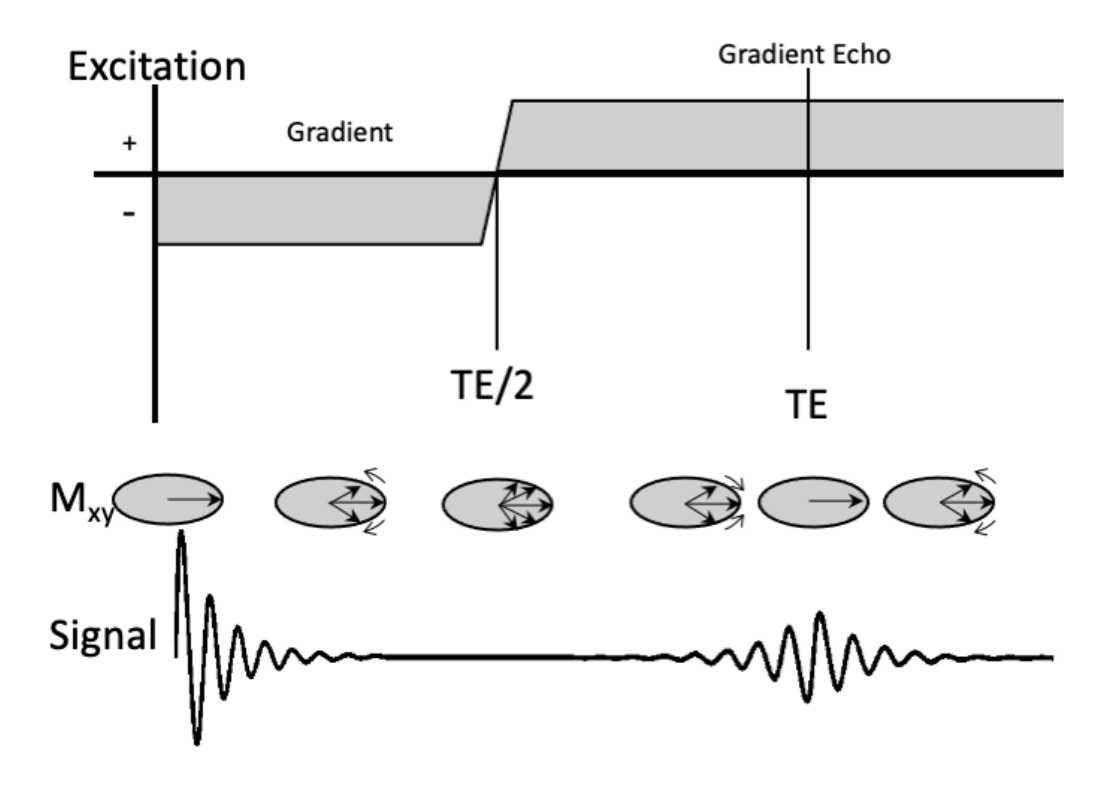


Figure 2-3: Basic Gradient echo pulse sequence showing the initial excitation from a small flip angle, followed by a gradient that is inversed and the resulting echo that is received, adapted from (17).

2.1.7 T_1 -weighted images

 T_I -weighted images are MR images that obtain contrast based on the T_I characteristics of tissues. Clinically, T_I -weighted imaging is usually done with spin-echo sequences that deemphasize T_2 and the magnitude of proton density contributions relative to the signal. These sequences have characteristics that include a short TR (~500 ms) to maximize differences in longitudinal magnetization recovery, and a short TE to minimize T_2 decay. Time (TR) between successive pulses maximize the signal difference between tissues based on their respective T_I values. The $\mathbf{M_z}$ of each tissue is converted to $\mathbf{M_{xy}}$ at each repetition, and to minimize T_2 decay and maintain differences in signal amplitude a short TE is used. For example, fat with short T_I has a large signal because of a greater recovery of $\mathbf{M_z}$ over the TR period. White and gray matter have

intermediate T_I values which results in an intermediate signal. T_I -weighted images can show gray matter white matter contrast. Cerebral spinal fluid has a long T_I and the lowest signal amplitude in T_I -weighted images, which can all be seen in Figure Figure 2-4

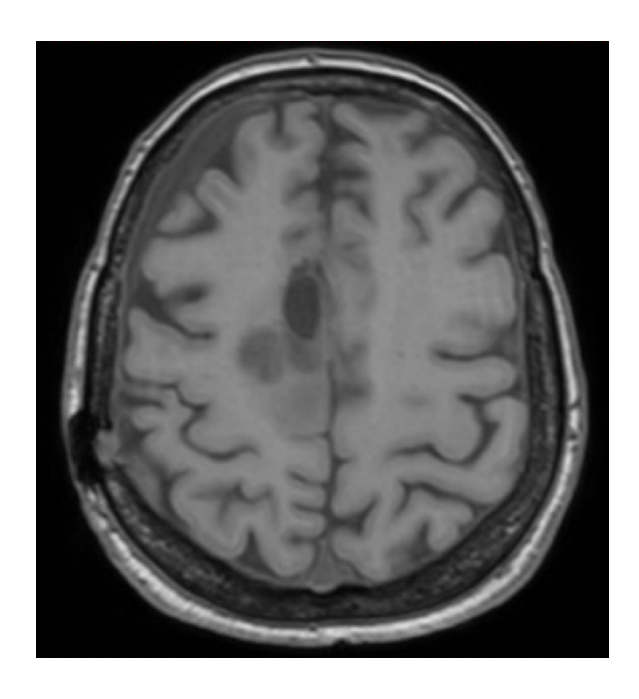


Figure 2-4: T_I -weighted image of the brain, from a patient with cancer of the brain. White and gray matter have intermediate T_I values which results in an intermediate signal. *Cerebral* spinal fluid has a long T_I and the lowest signal amplitude.

2.1.8 Gradient echo signals with short TR

A TR of less than 50 ms does not allow for transverse decay to fully occur (T_2 *) resulting in a steady state equilibrium of longitudinal and transverse magnetization from pulse to pulse. This is produced from previous RF signals and multiple signals are generated. These include: the FID signal at the end of each RF pulse, and the stimulated echo and spin echoes generated from the previous RF pulse. T_1 weighting cannot be achieved to a great extent due to the small difference in longitudinal magnetization with small flip angles. At large flip angles T_2 * effects dominate making T_1 weighting difficult. The effect of T_2 * can be reduced by "spoiling" the steady state

transverse magnetization through incoherent phase differences from pulse to pulse. This can also be done with gradient spoiling. This done by adding a phase shift to successive RF pulses. Since the RF transmitter and RF receiver are phase locked, the receiver discriminates the phase of the GRE from the SE generated by the previous pulse. Spoiled transverse magnetization gradient recalled echo (SPGR) is a common sequence in 3D volume acquisitions. It has a short TR and good contrast of anatomy provided by T_I -weighting. Contrast agents produce greater contrast with SPGR sequences than with comparable T_I -weighted sequences due to greater sensitivity to magnetic susceptibility. The signal from an SPGR will be explored further in section 2.2.1.

2.2 Dynamic Contrast Enhanced MRI

This section is an overview of relevant qualitative and quantitative techniques for analysis of contrast enhanced MRI.

2.2.1 Contrast Agents

DCE MRI requires a contrast agent which causes a signal enhancement by decreasing T₁ of nearby protons, through an indirect effect. The amount of signal enhancement is proportional to the concentration of the contrast agent of the tissue. The agent is typically injected intravenously, and thus, enhancement in tissues is also a function of perfusion characteristics. The effect of a contrast agent can be seen in

Figure 2-5. The lesion is significantly more visible in the post contrast frame. As we will see in section 2.4.3 this is due to leaky blood vessels formed during tumour angiogenesis.

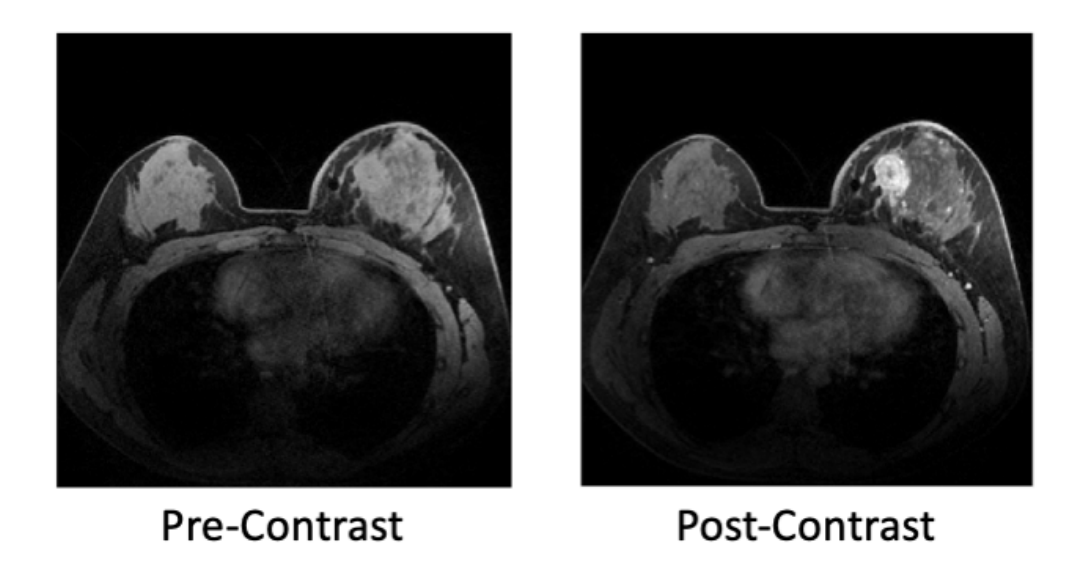


Figure 2-5: T_I -weighted image pre (left) and post (right) injection of the contrast agent. The enhancement of the lesion is apparent in the post contrast image. Data from (20).

The contrast agent in a tissue can be quantified in equation (10)

$$C_{tis}(t) = \frac{R_1(t) - R_{10}}{r_1}$$

(2-7)

 R_{I0} is the precontrast tissue relaxation rate, $R_{I}(t)$ is the tissue relaxation rate at time t, and r_{I} is the contrast agent's relaxivity constant. Here R_{I} depends on time since it is affected by the contrast agent whose concentration varies with time. For gadobutrol, a common gadolinium-based contrast agent, r_{I} is 4.7 mM⁻¹s⁻¹ at 1.5 T and 3.6 mM⁻¹s at 3.0 T (10). To quantify the contrast agent concentration a measurement of R_{I} is needed, but T_{I} -weighted images alone do not provide actual measurement and cannot be used to measure R_{I} . R_{I} can be obtained however, using 3D spoiled

gradient echo (SPGR). For this reason, SPGR is commonly used with DCE MR. The signal from SPGR is given by:

$$S(t) = S_0 sin\theta \frac{1 - \exp(-TR * R_1(t))}{1 - \cos\theta * \exp(-TR * R_1(t))}$$

(2-8)

Where θ is the flip angle, TR is the repetition time, $R_I(t)$ is the tissue relaxation rate at time t, and S_0 is the baseline MR signal, a combination of M_0 along with other factors associated with scanner electronics. This equation contains two unknowns (S_0 and $R_I(t)$). Thus, multiple images must be acquired at different fit angles, then S_0 and $R_I(t)$ may be solved using a system of equations. Pre contrast $R_I(R_{I0})$ must also be measured to be combined with $R_I(t)$, and there are approaches to do this with SPGR (21, 22). R_I quantification with multiple flip angles is possible but changing contrast agent concentrations makes acquiring multiple images per DCE-MRI frame not possible. One can circumvent this by first acquiring pre-contrast images using multiple flip angles and using those to calculate R_{I0} and S_0 . Then $R_I(t)$ can derived from equation (2-8) to get:

$$R_1(t) = -\frac{1}{TR} \ln \left(\frac{S(t) - S_0 \sin \theta}{S(t) \cos \theta - S_0 \sin \theta} \right)$$

(2-9)

Once $R_I(t)$ is obtained, the contrast agent concentration can be quantified at each timepoint using equation (2-9).

2.3 Shape Analysis in Dynamic Contrast Enhanced MRI

2.3.1 Shape analysis

Since contrast agents are administered intravenously, the DCE-MRI signal is a function of perfusion characteristics, so different voxels/tissues will have a different characteristic time-course curve shape. It turns out that even among voxels within lesions the curve shape varies and that some shapes can be indicative of malignancy (3). The most suspicious curve shapes usually have a sharp increase in signal followed by a rapid washout (23). Khalifa *et al* (24) proposed a classification of the shape types which can be seen in

Figure 2-6.

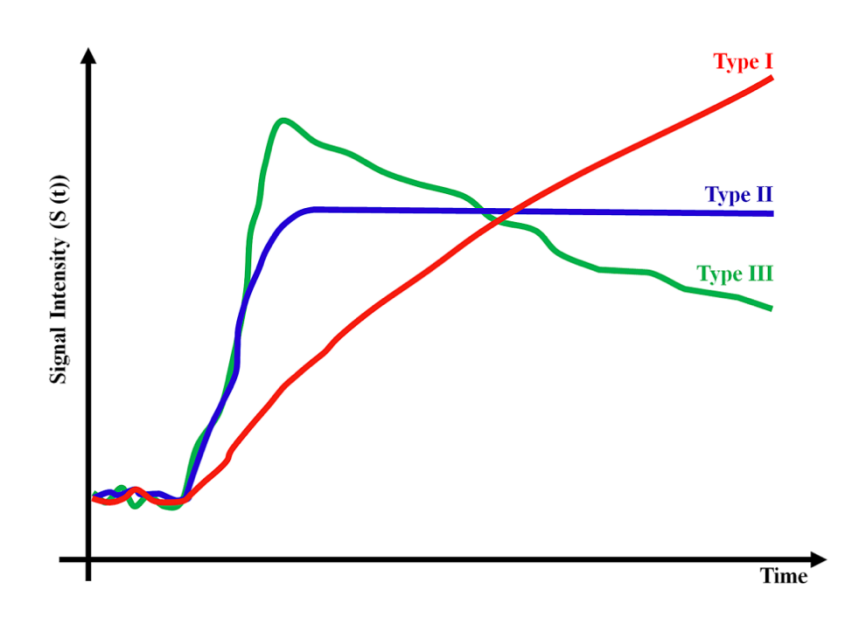


Figure 2-6: Proposed classification of shape types from Khalifa *et al* (24). Type I is characterized by persistent enhancement, type II characterized by an initial enhancement followed by a plateau, and type 3 is characterized by an initial enhancement followed by a washout.

There has been growing interest in identifying and classifying these shapes to classify lesions, known as shape analysis. The simplest method, is for an observer to visually look at the shape of the signal time curve in the tissue of image and classify them manually (23). Sometimes the tumours contain too many voxels, and only the most suspicious curves, or an average of many curves, are investigated (25) in the interest of efficiency. This can result in a loss of spatial information. Additionally, the classification is subjective as different individuals may classify shapes differently. A more in-depth look into shape analysis, its advantages and limitations can be found this review (3).

2.3.2 Semi-Quantitative Techniques

Signal time course curves have also been classified using semi-quantitative techniques. Semi-quantitative techniques include calculated parameters such as: area under signal-time curve, peak signal, time to peak and initial slope. One such method is the three timepoint (3TP) method (26). This involves acquiring images at 3 timepoints; pre injection, 2 minutes post injection and 6 minutes post injection. Time course curves were classified based on the difference between the second and third timepoint. Lavini *et al.* classified curves into 7 shapes using various features (27). Another way of classifying lesions that has had success in discriminating between benign and malignant lesions is using the enhancement rate of the curve, and the area under the curve from zero to each timepoint. (28).

Although these approaches seem promising, they are only somewhat comparable between scanners and patients. They are called semi quantitative because they do not account for things such as the injection protocol or systematic features of the scanners themselves. The injection protocol can vary between patients as the contrast agent dose is typically 0.1 mM/kg of body mass (29). Although higher concentrations would lead to a greater signal enhancement, the accuracy

would be worse because the relaxation rates would be so high the system relaxes completely between pulses, resulting in lesions that lose their visible structure and appear uniform. The peak concentration between two patients might not be comparable due to the difference in injection protocols. Despite this, semi-quantitative techniques have shown sensitivity to anti-angiogenic therapy-induced changes and extracting exact parameters may not be needed for this task (30). The same work concluded that semi-quantitative methods may even have an advantage over quantitative or pharmacokinetic methods in terms of noise tolerance.

2.3.3 Quantitative Techniques

Quantitative techniques aim to extract meaningful physical or biological characteristics such as flow (rate of blood supply volume per volume of tissue) or permeability (leakage of contrast agent from vasculature) that are comparability across protocols. These are essentially mathematical models that estimate physical characteristics by fitting pharmacokinetic models (a model that describes the movement of a drug throughout the body) to DCE data. Note that Gadolinium-based contrast agents are passive diffusing agents, so the pharmacological aspect is minimal (31). The computed characteristics are made comparable by including the injection protocol and other systematic features in the computational algorithms describing the data. They can include factors such as: injection speed, injected dose, scanning duration, systematic features such as the patient's heart rate. Most of these models are two-compartment models based on Kety's model (32). These include an intravascular compartment (plasma) and a peripheral compartment (extracellular extravascular space). There is an arterial input of the contrast agent to the intravascular compartment described by $C_a(t)$, and exchange can occur between the intravascular and peripheral compartments via rate constants k₁₂ and k₂₁. A visual diagram of this is shown in Figure 2-7.

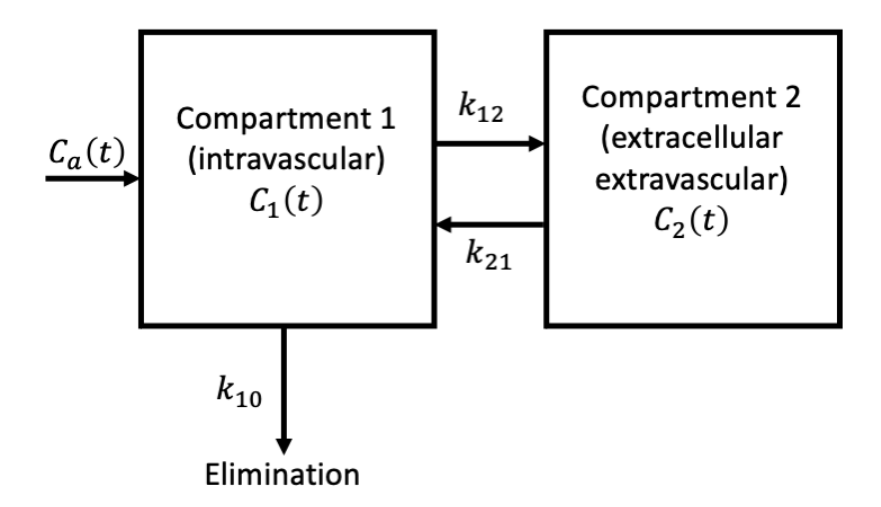


Figure 2-7: Visual representation of two compartment model. $C_a(t)$ described the arterial input into compartment 1. Exchange occurs between compartment 1 with concentration $C_1(t)$ and compartment 2 with $C_2(t)$ via k_{12} and k_{21} . Elimination occurs from compartment $C_1(t)$ via k_{10} .

It is common for models refer to $C_1(t)$ and $C_2(t)$ as $C_p(t)$ and $C_{tis}(t)$ respectively, and k_{12} and k_{12} as K^{trans} and k_{ep} respectively. The most common and simplest of these is the Tofts model (33)

$$C_{tis}(t) = K^{Trans}C_p(t) * e^{k_{ep}t}$$
(2-10)

Where there are two fitting parameters: K^{Trans} and k_{ep} . $C_p(t)$ is the amount of contrast agent in the plasma contained in the feeding blood vessel, also known as arterial input function. It accounts for the injection protocol and any systematic variations that may be present between patients or visits. It can be measured directly from blood extracted from arteries, approximated by a reference

tissue measurement, or replaced by a model or population average (24). The two fitting parameters can be related by another equation:

$$k_{ep} = \frac{K^{Trans}}{v_e}$$

(2-11)

Where v_e is the fraction of the voxel occupied by extracellular extravascular space. One major assumption of the Tofts model is that the feeding blood vessel occupies a negligible space in the voxel (34). This assumption does not hold for highly vascularized tissue such as the breast. This is addressed in the extended Tofts model (11) described by equation:

$$C_{tis}(t) = K^{Trans}C_p(t) * e^{(k_{ep})t} + v_pC_p(t)$$
(2-12)

Where v_p is an additional fitting parameter describing the fraction of the volume occupied by blood plasma.

Other such quantitative or pharmacokinetic models include: the Larsson model (12), where transfer between the intravascular and peripheral compartment is assumed to be reliant on a single rate constant, the Brix model (13), which includes several rate constants to describe the transfer of contrast agent between the intravascular and peripheral compartments, and the Patlak model (14), which uses a graphical approach to estimate the transfer rate constant between the two compartments. All of these have a single rate constant to account for both blood flow and permeability. The recent 2CXM model (15) includes many parameters for blood flow into the equation. For a more detailed breakdown of these models see a recent review by Khalifa *et al.* (24).

Temporal resolution of DCE-MRI can be a limitation in the accuracy of quantitative models. Henderson *et al.* (35) showed through simulations that in order to keep errors in estimation of k_{ep} and K^{Trans} under 10%, a temporal resolution of 16 s or lower is needed. Similarly, Larsson *et al.* (36) found that stable estimates of the aforementioned parameters were possible with a temporal resolution of 12 s.

2.3.4 Measuring the arterial input function

One critical component present in all of the of the quantitative models is the term $C_p(t)$ or arterial input function (AIF). This is the keystone that accounts for the injection protocol that allows for quantitative methods to be comparable across scanners and patients. Uncertainties or errors in the AIF can propagate leading to inaccurate pharmacokinetic parameters. The AIF can be measured directly or indirectly. The direct approach consists of drawing blood samples from the patient during DCE-MRI acquisition. This is accurate but has some drawbacks. The recommended temporal resolution is 15 seconds per sample (24). Measuring the AIF requires a temporal resolution of at least 5 seconds (35) to capture the initial peak. The indirect approach involves using DCE-MRI data in an arterial blood vessel to estimate the arterial input function. This has the advantage of not having a limit to the number of samples as it is not invasive. The spatial resolution must also be high enough to avoid partial volume artifacts in the feeding artery. This is particularly difficult in breast tissue where arteries may not be in view and feeding vessels are capillaries that may be as small as 200 µm (37). Measuring the contrast agent in blood through direct or indirect methods will provide the concentration of the contrast agent in the whole blood or C_{blood}(t). The contrast agent is constrained by red blood cells and not uniformly distributed in the whole blood. To calculate $C_p(t)$, one needs to correct for this using the equation:

$$C_p(t) = \frac{C_{blood}(t)}{1 - Hematocrit}$$

(2-13)

Where *hematocrit* is the fraction of the blood occupied by red blood cells. This requires measurement from a blood sample, or more commonly, the use of an assumed value which may not capture the possible variability of individual patients.

There are additional challenges to indirect approaches, manifesting as susceptibility to saturation effects, inflow effects, or improper RF spoiling. Saturation effects occur when the tracer concentration is higher than what the scanner electronics can detect. This can result in a truncated AIF peak (38). The blood inflow effect can have an impact on the sensitivity and accuracy of the AIF measured with DCE-MRI (39). The SPGR acquisition assumes that the imaged slice has a saturation of excited spins. However flowing blood can introduce a constant supply of fresh ¹H into the slice creating a partial saturation. This will affect the estimated T₁ and subsequently the contrast agent concentration.

One solution is the prebolus technique (40) which consists of two contrast agent administrations, the first a low-dose then a high-dose, and allowed for the accurate measurement of high concentrations of contrast agents without saturation effects. Phase induced AIFs are also a proposed solution, which do not rely on signal magnitude, instead measuring the intravascular phase shift, and would not be as sensitive to saturation or inflow effects (41, 42).

Reference region methods circumvent the need for measuring the AIF by using concentration time data from some well characterized tissue as a surrogate (43). The assumption is that the reference tissue and surrogate tissue have the same AIFs. This eliminates the measurement of the AIF, relaxing the need for high temporal resolution and therefore it becomes easier to have high spatial resolution

Model based approaches can be population-based AIFs which are published as functional forms. Commonly used models include; the Tofts-Kermode AIF (29), Parker AIF (44), Fritz Hansen AIF (45, 46), and Georgiou AIF (47). Tofts and Kermode fitted a bi-exponential equation to blood sample data to get:

$$C_p(t) = D \cdot (a_1 e^{-m_1 t} + a_2 e^{-m_2 t})$$

(2-14)

Where Tofts and Kermode determined that: D=0.1 mmol/kg, a_1 =3.99 kg/l, a_2 =4.78 kg/l, m_1 =0.144 min⁻¹ and m_2 =0.0111 min⁻¹. The main feature of this model is a single peak describing the passing of bolus. The Fritz Hansen model fit the bi-exponential but obtained different constants: D=1.0 mmol/kg, a_1 =2.4 kg/l, a_2 =0.62 kg/l, m_1 =3.0 min⁻¹, and m_2 =0.016 min⁻¹. The Parker AIF model was obtained from DCE data in the descending aorta to obtain:

$$C_p(t) = \frac{1}{1 - Hematocrit} \sum_{n=1}^{2} \left(\frac{A_n}{\sigma_n \sqrt{2\pi}} \right) e^{-\frac{(t-T_n)^2}{2\sigma_n^2} + \frac{\alpha e^{-\beta t}}{1 + e^{-s(t-\tau)}}}$$

(2-15)

Where $A_I = 0.809$ mmol·min , $A_2 = 0.330$ mmol·min $T_I = 0.17046$ min, $T_2 = 0.365$ min, $\sigma_I = 0.0563$ min, $\sigma_2 = 0.132$ min, $\alpha = 1.050$ mmol, $\beta = 0.1685$ min⁻¹, s = 38.078 min⁻¹, and $\tau = 0.483$ min. Here the curve has two peaks, one for the initial pass of the bolus and another for a recirculated second pass of the bolus, characterized by the two Gaussians in the function. The Georgiou AIF describes the initial passage and several subsequent recirculations of the bolus beyond just the first two described in the Parker AIF and used higher temporal resolution data to model the initial passing of the bolus more accurately.

Finally, averaged-AIFs are measured arterial input functions from patients that are averaged. They have been shown to be a useful alternative when patient specific AIFs are not available (38, 48). Both model based and averaged-AIFs have the same major limitation in that they cannot account for variability between patients. Finally the tissue from which the model was measured is also relevant: regions closer to the heart (i.e. head, neck, breast) have larger differences between individual patient AIFs, and may cause errors in calculated pharmacokinetic parameters (38).

Acquired parameters such as K^{Trans} or k_{ep} may not be accurate due to aforementioned limitations with model-based AIFs. However, the clinically useful components have been reported not to be the exact values themselves (49) but a change in the values in successive scans (49-51). A decrease in K^{Trans} represents a decrease in tumour vasculature (52). This is associated with the antivascular/antiangiogenic effects of the therapeutic agents to some extent (53). The changes in these parameters, which useful for monitoring changes that occur during chemotherapy, are still captured without ideal AIFs.

2.4 Breast Cancer Imaging

The section is an overview of the clinical role of MRI regarding breast cancer, including the techniques used and some technical requirements.

Breast cancer is the most common malignant disease with a lifetime risk of 12.4% for women (54). The following paragraph is a summary of a review by Rodney *et al* (55). Most breast cancers are carcinomas, which come from breast epithelial elements. There are two types: *in situ* carcinomas and invasive carcinomas. *In situ* carcinomas may start from either ductal or lobular epithelium but remain there, with a negligible chance for metastasis. If the ductal or lobular malignancy extends beyond the epithelial boundaries, it is considered invasive, where it has the

potential for metastasis leading to death from cancer. Prognosis of breast cancers depends on the stage, which includes tumour size and quantity of lymph node involvement. Breast conservation treatment is only appropriate for the majority of stage I and II cancers, as with those the survival is equivalent with a mastectomy. Radiation adjuvant therapy is routine after breast conserving therapy and mastectomies in order to prevent the recurrence of the disease. Adjuvant chemotherapy or hormone therapy may also be used to block cell growth (55). Neoadjuvant chemotherapy can be used to decrease the size of a tumour giving more surgical options, and MRI commonly used be used to monitor its effectiveness (1).

2.4.1 Breast MRI in Clinical Practice

Typically, mammography and ultrasound are used for detection, but have low sensitivity and specificity in dense breast tissues, and in the presence of breast implants or post-surgical scars (56). MRI adds additional diagnostic value in the form of: detecting foci of multifocal, multicentric or contralateral disease (57). MRI also performs better than mammograms at recognition of invasive components in ductal carcinoma in situ, and detection of cancer in dense breast tissue (58).

Breast MRI can also be used for screening, where MRI identified earlier stages of some diseases compared to mammography and that combined MRI and mammography is associated with improves survival rates (59).

Preoperative MRI for local staging is common, but the detection of more disease does not always lead to improved outcomes (60). Furthermore, guidelines differ widely in their recommendations. Size estimates with MRI are more accurate than those with mammography or ultrasound. Using breast MRI, 75 percent of cancers are measured within 1cm of their pathological size (61). Assessing tumour size is beneficial for invasive lobular carcinoma and the depiction of

DCIS components related to invasive cancers is better compared to mammography. However, improved information in staging does not always lead to improved surgical outcomes (1).

Clinical protocols are usually multiparametric and require a dedicated breast coil (59). Patients lie in the prone position with the breasts hanging in the recesses of the coil allowing for breast tissues to spread helping with detection of anomalies and reducing motion artifacts from breathing. These coils usually have 16 channels, to give a high signal-to-noise ratio.

Contrast enhanced MRI such as DCE-MRI enables assessment of morphological and kinetic patterns of benign and malignant breast tumours (1). DCE-MRI evaluates the permeability of blood vessels using an intravenous contrast agent. Neo angiogenesis leads to the formation of leaky vessels that allow for faster extravasation of contrast agent. This manifests as a rapid local enhancement.

2.4.2 Diffusion Weighted MRI

Diffusion Weighted Imaging is another MRI technique that is used to differentiate tumours. Motion sensitizing gradients are applied to quantify the random movement of water in tissues (62). The degree of water movement in biological tissue is restricted by intracellular compartments, extracellular compartments, and tissue cellularity. Decreased water diffusion manifests as a higher DWI signal. The apparent diffusion coefficient (ADC) is the quantitative measurement of DWI. Cancers have low signal intensity on ADC maps. Mean ADCs are generally higher in benign tumours (62). Contrast material injection does not improve the diagnostic properties of ADC (63).

2.4.3 Dynamic Contrast Enhanced MRI in breast cancer

DCE-MRI scans typically employ T_I -weighted images, which may be performed with or without fat suppression. They are usually acquired in the axial plane, as it is faster than sagittal

acquisition and provides a better overview. T_I -weighted images should be obtained prior to contrast material injection. The maximum administered Gadolinium-based contrast agent should be 1 mmol per kilogram of body weight, and there is no evidence for higher performance with higher dose (64, 65). Most breast cancers show peak enhancement around 60-90 seconds after contrast material administration, and so the after-contrast images must be acquired in this timeframe. Images acquired without fat suppression require subtraction images to be created from pre and post contrast acquisitions (66). Motion artifacts, chemical shift artifacts and poor fat suppression may obscure small lesions (67). Breast MRI should depict all enhancing cancers greater or equal to 5 mm in size. In order to meet this standard, section thickness should be less than 2.5 mm, and in plane pixel size should be 1 × 1 mm or lower (68). Modern MRI units can easily obtain higher resolutions than this with an acquisition time per volume of 90 seconds or less. One T_I-weighted image acquisition before contrast and one 90 seconds after contrast is sufficient for lesion detection, but more images can allow for breast lesion differentiation. One such is dynamic evaluation with time signal intensity curves. Dynamic evaluation documents the early inflow of contrast material in a lesion. Malignant lesions enhance, on average much later than benign lesions (69, 70).

Although T_1 -weighted imaging is mainly used in breast, T_2 -weighted imaging has some niche applications. T_2 -weighted imaging with fat suppression can be used to visualize cysts and imaging without fat suppression can allow for better depiction of lesion morphology. Some tumours such as mucinous carcinoma, necrotic cancer, and metaplastic carcinoma have high signal intensity with T_2 -weighted imaging (60).

Chapter 3: Analysis of Dynamic-Contrast-Enhanced MRI using Model-Based Classification Shapes

Alexandru Badalan¹, Zaki Ahmed^{1,2,3}, Marc-Antoine Fortin¹, Thomas Rosin², and Ives R Levesque^{1,2,4}

¹Medical Physics Unit, McGill University

²Department of Physics, McGill University

³Department of Radiology, Mayo Clinic, Rochester MN, USA

⁴Research Institute of the McGill University Health Centre

Montréal, Québec, Canada

Submitted for consideration as a Full Paper to Magnetic Resonance in Medicine

August 15, 2022

Statistics: 4379 words, 7 figures, & 0 tables on 21 pages, with 25 references

Address correspondence to:

Ives R. Levesque, PhD

Cedars Cancer Center – Glen Site, DS1.9326 Phone: (514) 934-1934 x.48105

1001 boul. Décarie Fax: (514) 934-8229

Montréal, QC, Canada, H4A 3J1 Email: ives.levesque@mcgill.ca

Running title: Model-based shape analysis for DCE-MRI

3.1 Abstract

Purpose: To introduce a method for shape-recognition analysis of dynamic contrast enhanced (DCE)-MRI that is rooted in quantitative modeling. The approach can be used to assess tumour perfusion. An application is demonstrated for the potential prediction of therapy response in patients with breast cancer.

Methods: The proposed method identifies the relative presence of pre-defined enhancement curves—based here on the Tofts-Kety model—in DCE-MRI data. The presence, or weight, of each of these curves in the data is estimated using a non-negative least-squares algorithm. In the example application, the weights were tested as markers of response to chemotherapy in a small group of patients with breast cancer.

Results: Shape analysis provided meaningful spatial information about tumour perfusion, and the dynamics in the time course data were captured using a relatively sparse set of model-based shapes. There was relation between therapy response and weights of the shapes in patients with breast cancer suggesting predictive ability and outperforming quantitative analysis in this respect. The method is robust to variations in implementation of the analysis.

Conclusions: A method was presented for analysis of DCE-MRI time course using predefined shapes based on the quantitative Tofts-Kety model. Our approach provides maps of the relative importance of perfusion characteristics such as slow and fast perfusion. The selection of predefined shapes, and the interpretation of the weight maps can be adapted to the specific application. Keywords: dynamic contrast enhanced MRI, perfusion, shape analysis, model-based shapes, nonnegative least-squares

3.2 Introduction

Characterization of tumour perfusion is an important clinical and research tool in the assessment of cancer. Dynamic contrast-enhanced (DCE) MRI exploits the dynamics of molecular contrast agents to study the perfusion characteristics of tissues and organs *in vivo* (24). The imaging consists of a series of T_I -weighted images acquired after a bolus injection of a gadolinium-based tracer. The uptake and subsequent washout of the tracer produces a time-dependent signal enhancement curve for each voxel. These curves can then be analysed further using qualitative, semi-quantitative, or quantitative methods.

Quantitative analysis of DCE-MRI has the advantage of providing physiologically meaningful information that is robust—in theory—to variations in scanner hardware, acquisition settings, and injection protocol (3). Quantitative analysis involves fitting a tracer-kinetic model, such as the well-established Tofts-Kety model (33, 71), to the acquired data. But, it is technically demanding since it requires 1) T_I mapping to convert signal into tracer concentration, and 2) knowledge of the arterial input function, *i.e.* the time-course of tracer in blood plasma (72). Questions have arisen around the reproducibility of quantitative approaches since the results depend on the software implementation for analysis (73, 74).

An alternative qualitative analysis method involves averaging the voxels in a region of interest and expert inspection of the average signal curve. This approach is popular because it is fast and technically simple. It has been successful in breast (4) achieving diagnostic indices of 91% sensitivity, 83% specificity and 86% diagnostic accuracy when evaluating the curve shape, and diagnostic indices of 91% sensitivity, 37% specificity and 58% diagnostic when evaluating the enhancement rate (the initial rate of growth of the time course curve following contrast agent administration). In soft tissue tumours (5) benign and malignant tissues were also able to be discriminated mostly based on the presence of liquefaction, time interval between start of arterial

and tumour enhancement, and lesion size. However, limitations of this approach include: the requirement for trained expert to select the region of interest that either contains the tumour, such that the results are operator-dependent, and it is too time consuming to employ on a voxel-by-voxel basis and therefore may fail to capture intra-tumoural heterogeneity.

To overcome the limitations of previous shape analysis work in DCE-MRI, automated approaches have been suggested that use semi-quantitative features of the signal curve to classify it into distinct categories based on curve shape. These shape classification approaches have found success in separating benign from malignant tumours in breast (9, 26) and soft tissue tumours (27). A major limitation is a lack of standardization. The classification shapes are arbitrarily defined and the number of shapes can vary from two to seven depending on the study (3). Furthermore, the specific criteria used for classifying the measured curves (*e.g.* maximum signal intensity, initial rate of enhancement, and time to enhancement) also differs between studies (3).

This paper introduces a method that uses a tracer-kinetic model – specifically, the Tofts-Kety model (75) – to define the classification shapes using a single parameter. We propose to analyze the observed signal enhancement time-curves as mixtures of the classification shapes. This decreases the number of classification shapes since many intermediate shapes can be generated as mixtures. We propose that this analysis technique can reliably distinguish regions of low and high perfusion, can be applied to data with low or high temporal resolution, and is robust to variations in the curve definitions.

In this work, we applied the technique to a freely-available dataset in breast cancer (76) to demonstrate its utility: in this portion of the work, we hypothesized that the analysis would have the same predictive ability as prior quantitative analysis of this data using the Tofts-Kety model.

3.3 Theory

In the proposed method, a set of classification shapes are pre-defined and identified in the measured time-course data using a fitting algorithm. The classification shapes are constructed using the Tofts-Kety model with parameter values taken from the literature. Prior work on the DCE quantitative model identified the k_{ep} parameter (the rate of contrast agent transfer from the interstitial space back to the plasma space) as the main determinant in the time-curve shape (16). Equation (3-1) is the Tofts-Kety model for the time-concentration curve, where C_t and C_p are the tissue and plasma contrast agent concentration, respectively, and K^{trans} and k_{ep} are the compartmental model parameters. The arterial input function (AIF), from which C_p is calculated, can come from a sample average or a model.

$$C_t(t) = K^{trans} \int_0^t C_p(\tau) e^{-k_{ep}(t-\tau)} d\tau$$
(3-1)

Once computed, the concentration-time curves are converted to signal-time curves s(t) considering the native tissue T_I (= $1/R_{1,0}$) and contrast agent relaxivity r_1 , according to equations (3-2) and (3-3), where s_0 is a coefficient which presents the theoretical signal amplitude of the fully relaxed magnetization, θ is the flip angle, and TR is the repetition time. The echo time (TE) is assumed to be short enough that R_2^* effects can be ignored. Each of these signal-time curves is then normalized to its maximum signal value such that the choice of s_0 is *ad hoc*.

$$R_{1}(t) = R_{1,0} + r_{1}C_{t}(t)$$

$$s(t) = s_{0} \frac{1 - e^{-\text{TR} \cdot R_{1}(t)}}{1 - \cos(\theta) e^{-\text{TR} \cdot R_{1}(t)}} \sin(\theta)$$
(3-2)

Each parameter in the compartmental model impacts the shape of the concentration-time curve differently, as illustrated in Figure 1 (top). The noteworthy observation is that a constant k_{ep} results in a set of curves with the same basic shape, as expected since it is the rate constant of the impulse response of the system. Therefore, a set of shapes (with normalized amplitude) can be defined using unique values of k_{ep} as the shape parameter. A set of resulting normalized signal curves for 5 k_{ep} values are plotted in Figure 1 (bottom), underlining the role of k_{ep} in determining the signal curve shape.

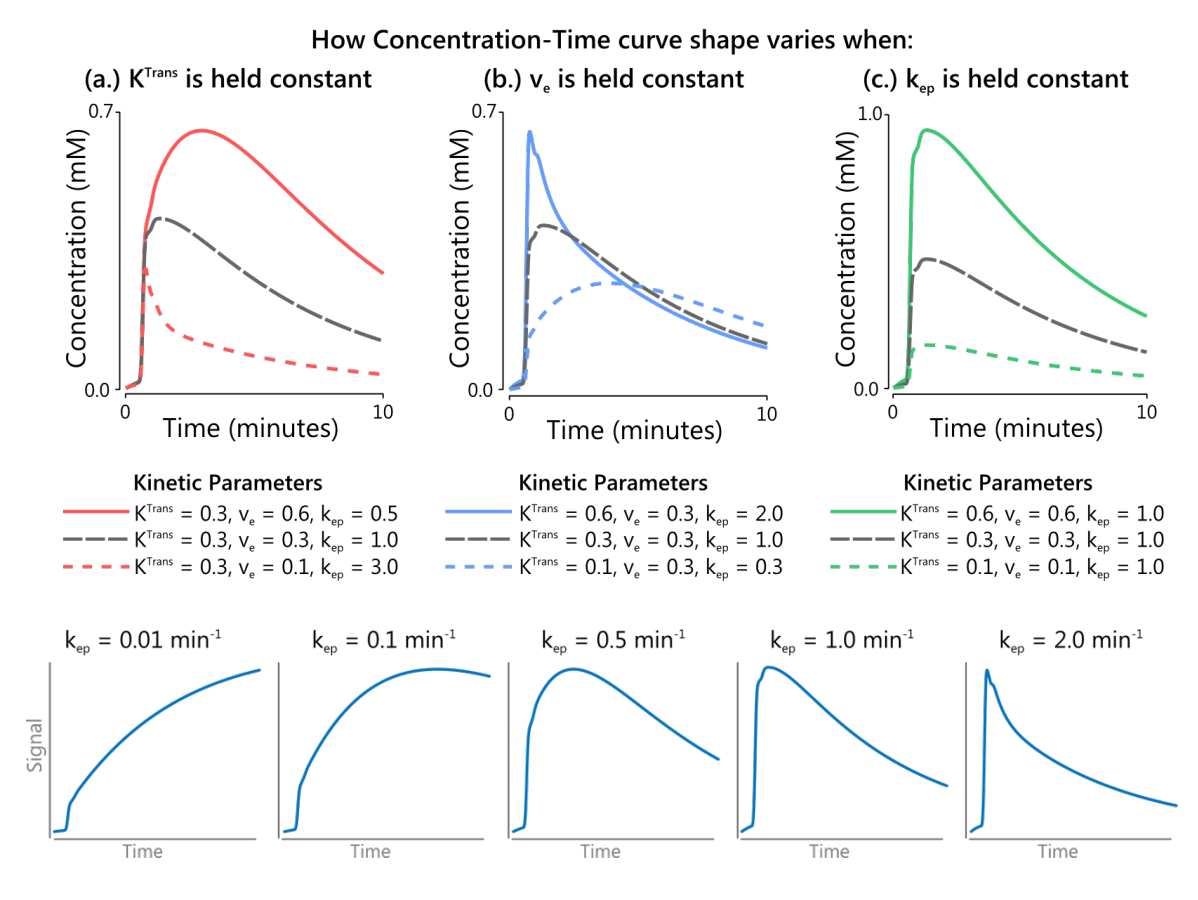


Figure 3-1: Top row: Calculated model curves for the Tofts-Kety model, illustrating the impact of variations in each of the model parameters. Note that for the case of constant k_{ep} , the model shape is essentially constant. Bottom row: Calculated model curves for the Tofts-Kety model for a wide

range of k_{ep} values, showing the wide range of shapes that can be produced, from very slow and persistent enhancement (very low k_{ep}) to very fast, sharply declining enhancement (very high k_{ep}).

The classification method assumes that signal time-curves in the acquired data are weighted mixtures of the predefined shapes. The number of curves is left as a choice to the user and can be based on a priori information about the data on hand. The problem of determining the weights can be represented as in equation (3-4), where y(t) are the measured data points and the $s_i(t)$ are the predefined curves. The weights w_i are computed using non-negative least squares (NNLS), details of which are described elsewhere (77). The NNLS algorithm returns the strictly positive weights that result in the best combination of the shapes to fit the data.

$$y(t) = \sum_{i} w_{i} s_{i}(t) + \epsilon$$

(3-4)

Prior to estimation of the weights, the data are pre-processed. First, the background signal is removed by subtraction of a pre-contrast frame, to isolate the enhancement. Finally, these voxel-wise signal enhancement data are normalized to the maximum enhancement signal in the tumour.

3.4 Methods

3.4.1 Simulations

Experimental simulations were performed to evaluate the sensitivity of the proposed method to a range of theoretical input curves. This helped address the question of the number of individual curves to use in the analysis. Simulated time-intensity curve data were produced using the Tofts-Kety model over a range of k_{ep} values from 0.001 to 1.0 min⁻¹, in steps of 0.001 min⁻¹. A temporal resolution of 0.5s was used in this simulation. The curves were then processed using the

proposed shape analysis method to assess its behaviour in reflecting the underlying data characteristics. Up to 5 predefined model curves were used, and the values of the weights and the goodness-of-fit were measured.

A second set of calculations explored the impact of modifying the temporal resolution of the acquired time course data on the analysis. The set of simulated enhancement time-course curves previously generated using the Tofts-Kety model was downsampled to temporal resolutions of 1, 5, 10, 30, and 60 seconds before being analyzed with a two-component model. The effect of temporal resolution was assessed by comparing the weights from the shape-recognition analysis and the fitting residuals normalized by the number of datapoints.

3.4.2 Experimental

To demonstrate the shape-based DCE-MRI analysis method, it was applied to patient data from the freely available "QIN Breast DCE-MRI" dataset from the Cancer Imaging Archive (12). This is a dataset acquired from 10 patients with breast cancer who underwent neoadjuvant chemotherapy, at two time points (pre-treatment and following one cycle of therapy). In the original work with this data, quantitative DCE-MRI analysis was moderately predictive of pathological response to neoadjuvant chemotherapy at pre- and intra-treatment MRI exams. Our hypothesis was that the shape-recognition weights that characterized the perfusion characteristics of these tumours would be different for patients showing pathologic complete response (pCR) from those of non-pCR patients, at one or both imaging time-points. Among these patients, 3 showed pCR. We used images from the pre-treatment exam (visit 1) and after the first cycle of treatment (visit 2).

In analyzing the breast cancer dataset, we designed our model shapes using k_{ep} values from Eliat *et al.* (78) to define two concentration-time curves described as low permeability ($k_{ep} = 0.27$ min⁻¹) and high permeability (k_{ep} ,= 0.90 min⁻¹) values reflecting benign and malignant tumours,

respectively. The Eliat study reported K^{Trans} and v_e such that k_{ep} was calculated using $k_{ep} = K^{trans}/v_e$. NNLS analysis was used to compute the weights voxel by voxel and we evaluated whether the mean weight of non-zero voxels (denoted as "MeanNZ") in the tumour ROI can predict therapy response. We used patient-specific T_I values (ranging from 1600 ms to 2500 ms) and the AIF provided in the "QIN Breast DCE-MRI" dataset to define classification shapes.

We also repeated the experiment with *in vivo* data using k_{ep} (curve-shape) parameter values from other studies, namely Furman-Haran *et al.* (79), Tofts *et al.* (75), and Vincensini *et al.* (80) studies. The values used and generated curves can be seen in Figure 3-2.

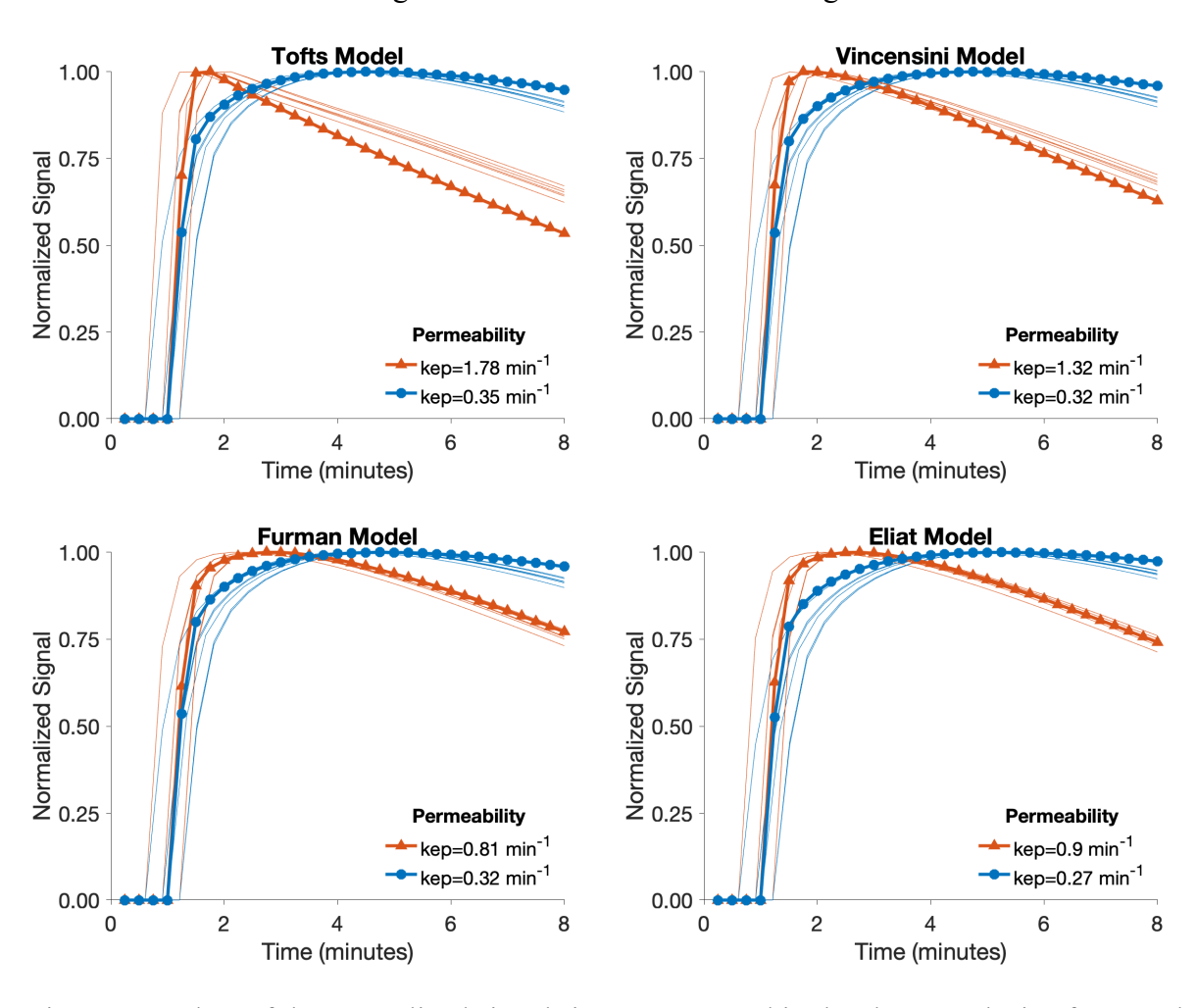


Figure 3-2: Plots of the normalized signal-time curves used in the shape analysis of *in vivo* breast cancer data. The thicker lines are shapes are calculated using the Tofts (75), Vincensini (17), Furman (15) and Eliat (78) studies with the Parker AIF and $T_1 = 1.81$ ms. The faint lines are patient

specific shapes calculated using AIFs and T_1 provided with the dataset. Symbols are included to illustrate the data time-points.

Using the same *in vivo* data, we evaluated whether the observations of the proposed method were sensitive to variations in the T_I value or the AIF time-course used to construct the pre-defined shapes. We repeated the analysis using shapes defined with fixed T_I values of 1000 ms and 100 ms (instead of patient-specific T_I values). We also performed the analysis with the patient-specific T_I and shapes defined using the population-based AIF model and parameters from Parker *et al.* (44) and finally with a combination of the Parker AIF and $T_I = 1000$ ms.

The analysis was also performed with three curves: the two original curves, plus the AIF as an extra curve. The Tofts-Kety model assumes that the volume occupied by blood vessels is negligible in every voxel, which may not be true for highly vascularized tissue such as the breast. Simulations have shown that the Tofts-Kety model is not accurate in highly vascularized tissues (34) and that the Extended Tofts Model (71), which includes an additional AIF term, is more accurate in highly perfused tissues. Thus, the inclusion of an AIF curve may lead to a model that better fits the data.

For all variations of the *in vivo* experiments, the weight maps were analyzed by looking at descriptive parameters like the mean, median, and standard deviation. Univariate analysis was used to determine if the weight map parameters were related to treatment outcome. The area under receiver-operating characteristic (AUROC) curve was used to measure and compare predictive power of the shape analysis method with the aforementioned variations.

The goodness-of-fit of the model was assessed in each voxel. The model curve was generated by scaling the low and high perfusion components by their respective weights. The residuals and coefficients of determination (R²) between the model and the data were calculated for each voxel. They were analyzed by looking at their mean, median, standard deviation, and their distribution

on histogram plots. The R² values of individual voxels were plotted in histograms to visualize their distribution.

3.5 Results

3.5.1 Simulations

Simulations revealed that the algorithm consistently models a signal based on an underlying Tofts-Kety two-compartment model with a mix of two shapes, at most. This result was independent of the number of pre-defined shapes in the analysis, and models with up to 6 shapes were tested. When using two shapes, the algorithm uses a mixture of the two only when the shape of the underlying data is characterized by a k_{ep} between that of the two curves (Figure 3-3). When the algorithm is used with three shapes, only two are assigned non-zero weights for any given data (Figures. 3-3 and 3-4). The algorithm maintains this behaviour with more shapes (Figure. 3-4).

Interestingly, temporal resolution had very little impact on the analysis results. When using two shapes and varying the temporal spacing of the simulated input data from 1 second to 60 seconds, the calculated weights barely changed. The goodness-of-fit was affected slightly. The normalized fit residuals were always below 1% per point for simulated data curves with k_{ep} between the values used in the two-component model. Normalized fit residuals increased for data outside the range covered by the two k_{ep} values, and the increase was greater for low-temporal-resolution data, up to 6.5% per point at 60-second temporal resolution.

3.5.2 Experimental

In vivo data were analyzed with two pre-defined shapes, calculated using $k_{ep} = 0.27 \text{ min}^{-1}$ for low perfusion and 0.90 min⁻¹ for high perfusion from the Eliat Model. These k_{ep} values were selected to reflect perfusion levels characteristic of benign and malignant disease (78). The resulting shapes were previously shown in Figure 3-2.

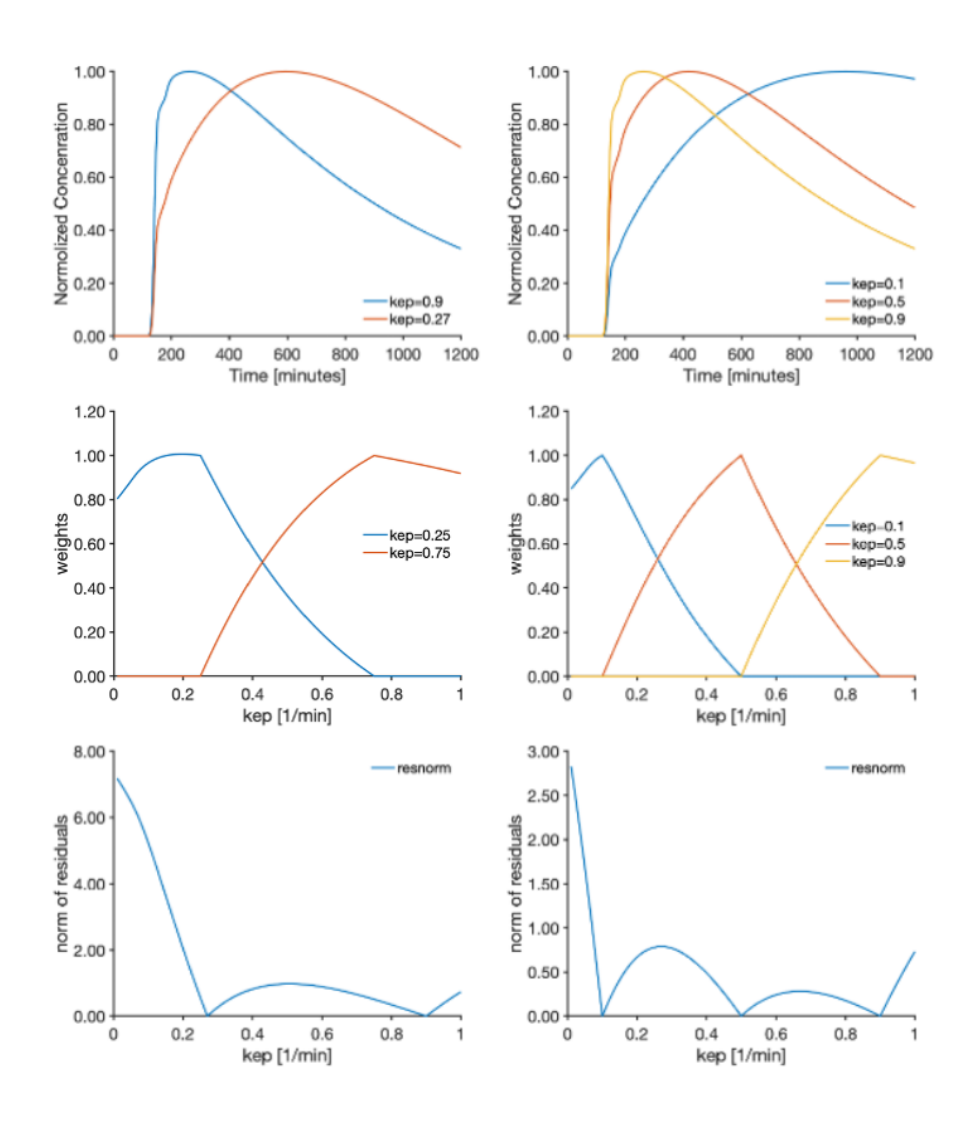


Figure 3-3: Simulation results from fitting single-component Tofts-Kety model curves using two (left column) and three (right column) pre-defined analysis shapes. Top row: the shapes (with associated k_{ep} values). Middle row: weights resulting from the analysis. For a range of input (theoretical) model k_{ep} values from 0.001 to 1.0 min⁻¹ the model only ever returns non-zero weights for at most two of the pre-defined shapes. The weight assigned to a given curve peaks at the k_{ep} value of the curve. Bottom row: fitting residuals. The residuals are lowest at or between the k_{ep} of the pre-defined analysis shapes, suggesting that the minimum and maximum k_{ep} values should cover the expected range of shapes.

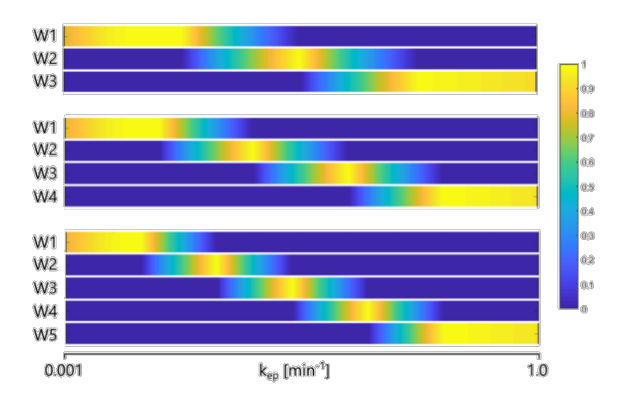


Figure 3-4: Effect of varying the number of reference curves (sources) used in weighted fitting on the analysis for 3, 4, and 5 sources. Shows that for any given input curve from a single k_{ep} value, the analysis method uses at most two pre-defined curves with distinct k_{ep} values in the fit. Simulations were performed with up to 5 curves producing results leading to the same conclusion.

The weight maps clearly display distinct areas of signal that reflect the location of the tumour. These distinct areas varied between patients. The low and high perfusion weight maps highlight different areas of the tumours. Normal tissue generally had high fitting residuals and very low weights for both components, indicating that the model did not recognize it as low- or high-perfusion tumour (based on the definition of the shapes in the analysis). The appearance of the weight maps was different between patients showing pathologically complete response (N=3) and those who did not (N=7). Examples from two patients in each group are shown in Figure 3-5, highlighting the difference especially in high perfusion content. Tumours that were later identified as complete responders had smaller amounts of high perfusion weights (green) at visit 2 than the non-complete responders.

There was a clear relationship between therapy response and the mean value of the weights over all pixels with non-zero weight values ("MeanNZ"), from the low perfusion channel at visit 1 (pre-treatment) and the high-perfusion channel at visit 2 (after 1 cycle). The MeanNZ for the low-permeability shape at visit 1 and for the high-permeability shape at visit 2 were both able to

separate pCR from non-pCR patients (Figure. 3-6, Standard). The high-permeability shape at visit 1, and the low-permeability shape at visit 2, did not have predictive value.

Incorporating the AIF as a separate time-course in the model did not lead to meaningful improvement in the R^2 values of the fit or in the predictability of therapy response.

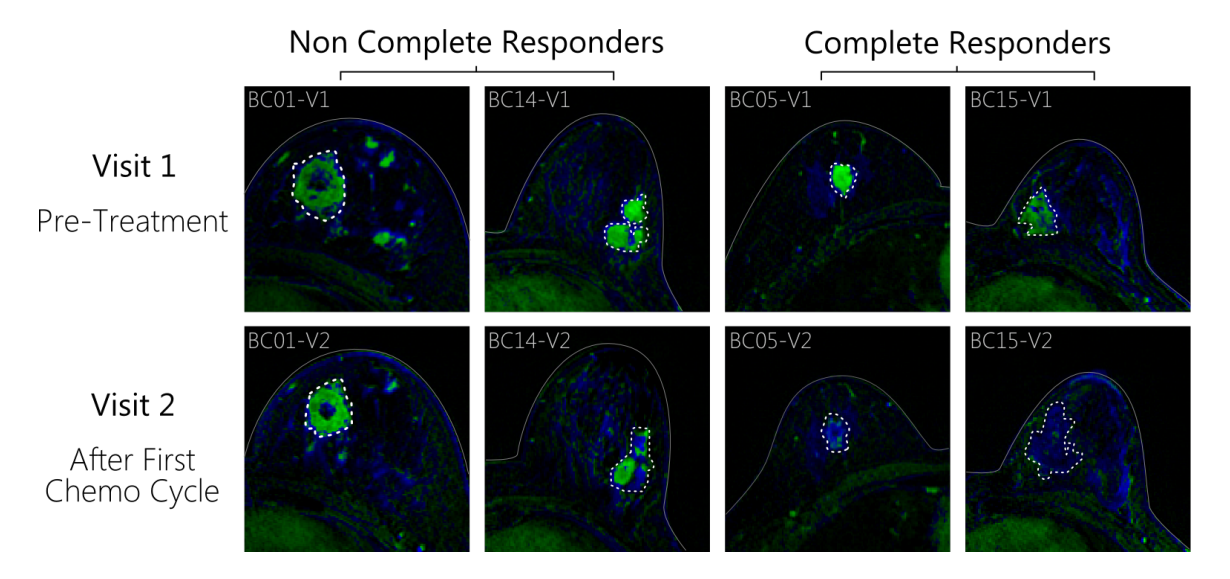


Figure 3-5: Fused weight maps for two-shape (low/high) perfusion analysis. The low perfusion weight is represented by the intensity in the blue channel, while the high perfusion weight is in the green channel. In these data from breast cancer patients (freely available from TCIA (76)) there appears to be a pattern of perfusion that reflects response to treatment.

Tests of the robustness of the algorithm on patient data revealed that it is quite robust to most of the assumptions made in defining the source time-curves. Modifying the T_I value used in this calculation did not impact the results unless the estimated T_I was assigned a low value (< 100 ms), suggesting the T_I value assumed in the curve definitions does not affect results (within a reasonable range) and that T_I mapping is therefore unnecessary. Overestimation of the T_I value did not have an impact on the assigned weights for high perfusion component at visit 2, and a slight impact on the weights of the low perfusion component at visit 1. The separation based on therapy response was not impacted by the T_I selection. These results are shown in Figure 3-6 (" T_I = 1000ms", " T_I = 100ms")

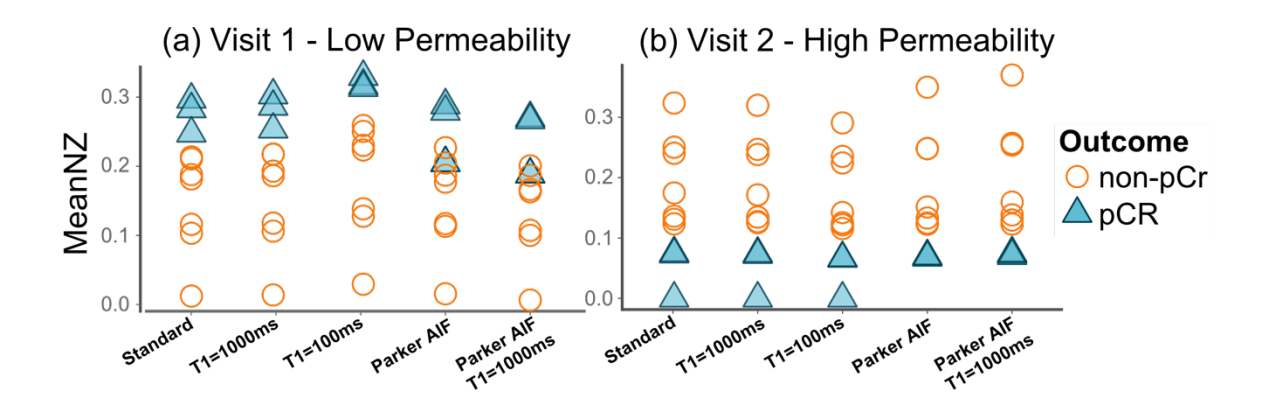


Figure 3-6: The mean values of the weights from the two-component analysis of *in vivo* data can distinguish between patients depending on their pathological response. The distinction is observed on the low-permeability weight at visit 1 in panel (a) (pre-therapy), and the high permeability weight at visit 2 in panel (b) (after 1 cycle of chemotherapy). The analysis is also quite robust to the choice of T_1 value and AIF used in the definition of the analysis shapes, suggesting that the method is quite robust. The area under the ROC curve is 1 for all cases except two: at visit 1, using the Parker AIF to define the shapes.

The choice of the arterial input function (AIF) had a noticeable effect on the pre-defined shapes, and this altered the discrimination power of the analysis on this dataset. This can be seen in the two right-most columns of Figure 6 ("Parker AIF", and "Parker AIF, T_I =1000ms"), where the discriminatory power is much reduced. The area under the receiver operating characteristic curve (AUROC) is 1 for all but these two cases in Figure 6a, and all cases in Figure 6b; however, the AUROC drops to 0.952 for the low permeability shape at visit 1 when Parker's population-based AIF is used in defining the source shapes.

The distribution of R² values between the model fit and data for individual voxels for non-pCR in visits 1 and 2 were similar and mostly around 0.9, showing that the model fits the data well in general. The distribution of R² values for pCR patients is around 0.9 as well for visit 1 but is centered around 0.7 for visit 2. These can be seen in Figure 3-7. There was also a high number of

counts in the 'zero' bin for non-PCR patients. These zero values come from a single patient and are associated with a non-enhancing region in the center of a large tumour.

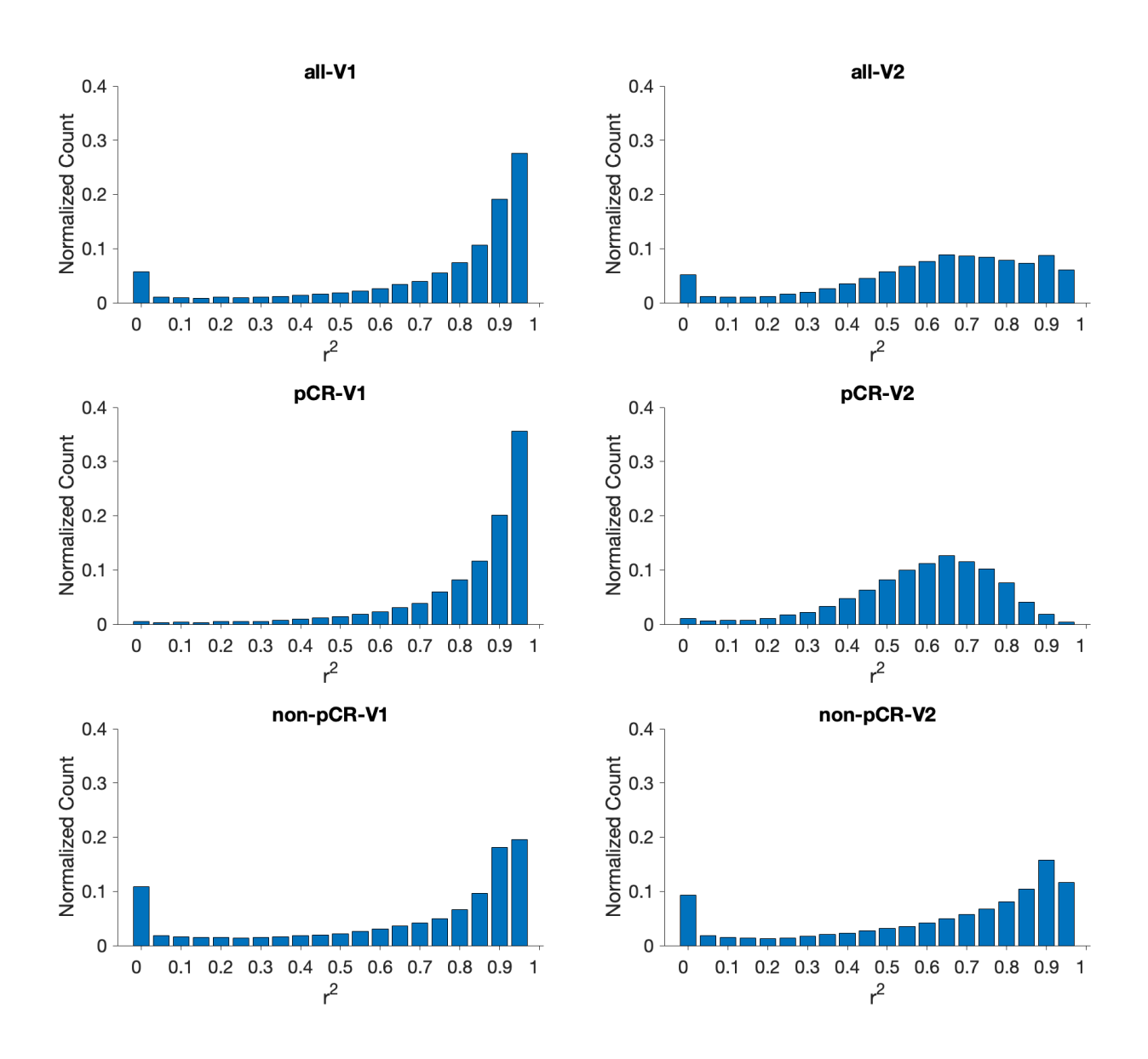


Figure 3-7: Histograms of the R^2 values of individual voxels from shape analysis with k_{ep} parameters from the Eliat model. The patients are separated in to pCR and non-pCR visits 1 and two, as well all visit 1 and all visit 2. Shape analysis done on pCR-visit 2 scans are the only ones that do not have R^2 values centered around 0.9, indicating that the model fit is not as good.

3.6 Discussion

In this work, we have introduced a novel technique for shape-based analysis of DCE time-courses, and more importantly have shown that this method may have predictive value in assessing the response of breast cancer treated with neoadjuvant chemotherapy. The discrimination between pathologically complete response and non-response was very strong across a range of analyses. This surprisingly strong result must be taken with some reservations, as it was obtained in a small dataset. In addition, certain modifications to the analysis reduced the discriminatory power of the method, reducing the area under the receiver-operating curve for the predictive value of pretreatment imaging from 1.0 to 0.952.

The original study on this dataset had shown that responders and non-responders could be separated based on DCE-MRI parameter values of k_{ep} and K^{Trans} following their first course of treatment and on the change in k_{ep} and K^{Trans} between visit 1 and visit 2 imaging. The highest pretreatment AUROC was reported as 0.857 (76). Interestingly this is lower than the lowest AUROC of 0.952 from our shape analysis method. These results strongly suggest that shape analysis of perfusion MRI based on representative quantitative model curves could be a powerful analysis tool for prediction or early assessment of treatment response.

MRI based on representative quantitative model curves could be a powerful analysis tool for prediction or early assessment of treatment response.

In addition to the clinical data, shape analysis was run on a set of simulated DCE-data generated using an underlying two-compartment Toft-Kety model. Running shape analysis on this simulated DCE data revealed that regardless of how many shapes were used, each simulated input time course was described by a maximum of two shapes with non-zero weights. This reflects the behavior of NNLS, which prefers to select sparse solution with as few non-zero solutions as

possible (81). This suggests that two shapes would be sufficient when considering how many initial source shapes to select when using NNLS.

Our shape analysis approach avoids the limitation of quantitative model DCE analysis that requires high temporal resolution for a good fit. Accurate fitting of such models requires a temporal resolution of 5 seconds or better (82), while most clinical protocols have a temporal resolution of 15–90 seconds (68). As a result, Tofts-Kety model analysis is usually limited to research. However, the minimal effect of temporal resolution on the goodness-of-fits in the simulation our method suggests that our method can be applied to clinical data of lower temporal resolution.

Analysis of the goodness-of-fit showed the R^2 value decreasing for responders at the second visit. This suggests that the model does not describe the data as well. We speculate that this caused by changes in the tumor microenvironment. Additionally, the shape analysis model fails to describe normal tissue and non-enhancing (perhaps necrotic) tumour tissue, assigning weights close to zero for both shapes and resulting in very poor fit reflected in low R^2 values.

A potential limitation of this technique is that the parameter values used in predicting therapy response were not necessarily designed for this kind of assessment. For example, Vincensini had reported k_{ep} values that were indicative of tumour histological subtype. We applied the parameters from this study to predict therapy response. The same question can be asked for models where reported values were indicative of benign/malignant classification. It may possible that our method predicts tumour subtype or grade, and that subtype or grade predicts therapy response.

In addition to tumours and tumour grading, shape analysis can also be used to assess the activity of inflammatory processes (83) and even the effect of drugs (84). Although the most common application has been in breast, studies have also been done in other tissues including, liver, brain, prostate, and abdomen (27). Thus, the selection of predefined shapes and interpretation

of weight maps from the proposed method is not limited to only breast tumours and can be adapted and applied to other types of analyses.

The main goal of this work was to design a method with clinical utility to analyze DCE-MRI data, but this method has potential to be applied as a research tool as well. One way could be to obtain data-based curves by using methods such as clustering, and then using NNLS to find weight maps for the cluster centers. This is different from current clustering methods which try to extract parameters from the clustered curves.

Other methods of analysis include analyzing the tumours through image segmentation or texture analysis or voxel wise changes but did not achieve the same performance as quantitative Tofts-Kety model or shape analysis in this dataset. Analysis of voxel wise features such as tumour deformations achieved an AUROC of 0.73 as predictors of therapy response in breast cancer (85). A prediction model based on a combination of clinical information, subjective radiological findings, and first- and second-order texture features achieved an AUROC of 0.78 for therapy response in breast cancer (85).

One limitation of this method includes the availability of an arterial input functions for use in our model. The dataset used in this study included an averaged arterial input function determined from signal time course of 3 patients (86). To test the robustness, we ran the analysis using the Parker functional form AIF. The result was an AUROC lower than with the AIF included with the data. This is a limitation for datasets where a direct or population averaged AIF is not available, and functional forms are necessary.

Another limitation of the method is the need for contouring the lesions. The data set used in this study contained regions of interest with lesions manually delineated by experts. Manual contouring is a time-consuming process, requires expertise to perform, and is likely to be operator-

dependent. One solution would be to implement an algorithm to automatically contour the tumors, and this solution is employed in some quantitative studies with moderate success (87). These algorithms can involve selecting the voxels with the highest enhancement, selecting all voxels over a threshold of enhancement, or selecting an area around the highest enhancement voxel.

3.7 Conclusion

Shape analysis allows for the analysis of DCE-MRI data using predefined shapes based on the quantitative Tofts-Kety model. It uses NNLS to classify measured time course data as mixtures of shapes. It is fast and robust to variations in flip angle and T_I . In a DCE MRI dataset from 10 patients with breast cancer, shape analysis was able to identify complete responders prior to treatment and after one cycle of neo-adjuvant chemotherapy, outperforming previously established quantitative analysis based on the quantitative Tofts-Kety model. This method could be a powerful tool in early assessment of treatment response. The selection of predefined shapes and the interpretation of weight maps can be adapted to the specific application.

3.8 Acknowledgments

The authors acknowledge the input of colleagues Véronique Fortier, Caroline Reinhold, Jan Seuntjens, Mikaël Simard, Martin Vallières, and Stella Xing in discussing this work. Funding was provided by the Research Institute of the McGill University Health Centre (Montreal General Hospital Foundation) and a Discovery Grant from the Natural Science and Engineering Research Council (NSERC). ZA acknowledges fellowship funding from the NSERC CREATE Medical Physics Regional Training Network (Grant no. 432290) and the McGill University Faculty of Medicine Fellowships.

Chapter 4: Further Analysis with Additional Shape Types and Automatic Tumour Delineation

4.1 Shape Analysis with 3 input shapes

4.1.1 Introduction

Vincensini reported k_{ep} parameters that reflected breast tumour subtype (80) which were used for shape analysis in Chapter 3. These subtypes were invasive ductal carcinoma (IDC), invasive lobular carcinoma (ILC) and benign tumours. The k_{ep} parameters used in this study were applied to predict therapy response, and the results reported in Chapter 3 suggest that time-intensity curves decomposed using our method based on published k_{ep} values are related to outcomes. This brings about an interesting question of whether these k_{ep} parameters be used to determine tumour subtype, or are they only useful for predicting therapy response.

As described in sections 2.4 Invasive lobular carcinoma is the second most common type of breast cancer (88). Its clinical, biological, and prognostic values make it a separate entity from invasive ductal carcinoma (IDC). Patients with IDC were more likely to experience pCR when undergoing neoadjuvant chemotherapy compared to ILC (89).

Tofts also proposed an extension to his model for tissue that is highly vascularized (11). This is expanded on in greater detail in Chapter 2. The Extended Tofts model consists of adding an additional term containing the arterial input function multiplied by the fraction of the voxel occupied by blood vessels. Conceptually, this is similar to having the AIF as a third shape component in shape analysis that can have a weight in each voxel.

The objective of the work presented in this chapter was to investigate whether additional input shapes on the shape-based analysis improves the outcome of the analysis. This was first done with 3 shapes derived from 3 k_{ep} values reported by Vincensini *et al*. Then the analysis was repeated with 2 shapes from k_{ep} values from Eliat *et al*, as was done in Chapter 3 and the Parker AIF (44) component as a third shape.

4.1.2 Methods

Shape analysis was run using 3 shapes instead of 2, with the parameters being taken from Vincensini *et al*. Vincensini *et al* k_{ep} values for IDC, ILC and benign tumours which were 1.32 min⁻¹, 0.66 min⁻¹, and 0.32 min⁻¹ respectively (80). In the previous analysis reported in Chapter 3, values of 1.32 min⁻¹ and 0.32 min⁻¹ k_{ep} were used for the high and low shapes respectively. The mean value of the weights over all pixels with non-zero weight values were compared at each of the visits to see if the separation seen before was maintained. Separation was quantified by calculating AUROC.

Shape analysis was also run using 2 shapes based on values from the Eliat study (78), and the average AIF supplied with the dataset as a third shape. The mean value of the weights over all pixels with non-zero weight values were compared at each of the visits to see if the separation seen in section 3.5.2 was maintained. Separation was quantified by calculating the AUROC.

4.1.3 Results

Following analysis of the dataset with three k_{ep} shapes describing breast cancer tumour type, the separation (AUROC = 1) at visit 1 is maintained by inspection of the mean non-zero weights of the highest k_{ep} shape (1.32 min⁻¹) which was the k_{ep} value for IDC. In this case, in contrast to the result observed in section 3.5.2 the separation at visit 2 is reflected in the intermediate k_{ep} (0.66 min⁻¹), which was the k_{ep} value reported for ILC. R^2 values are also slightly

higher than the 2-shape analysis from section 3.5.2. The lowest k_{ep} shape (benign) no longer separated pCR and non-pCR patients. This is shown in Figure 4-1. The 2-shape analysis in Chapter 3 had mean R² values of 0.81 and 0.70 for visit 1 and visit 2 respectively, while the 3-shape analysis had R² values of 0.82 and 0.71 for visit 1 and visit 2 respectively.

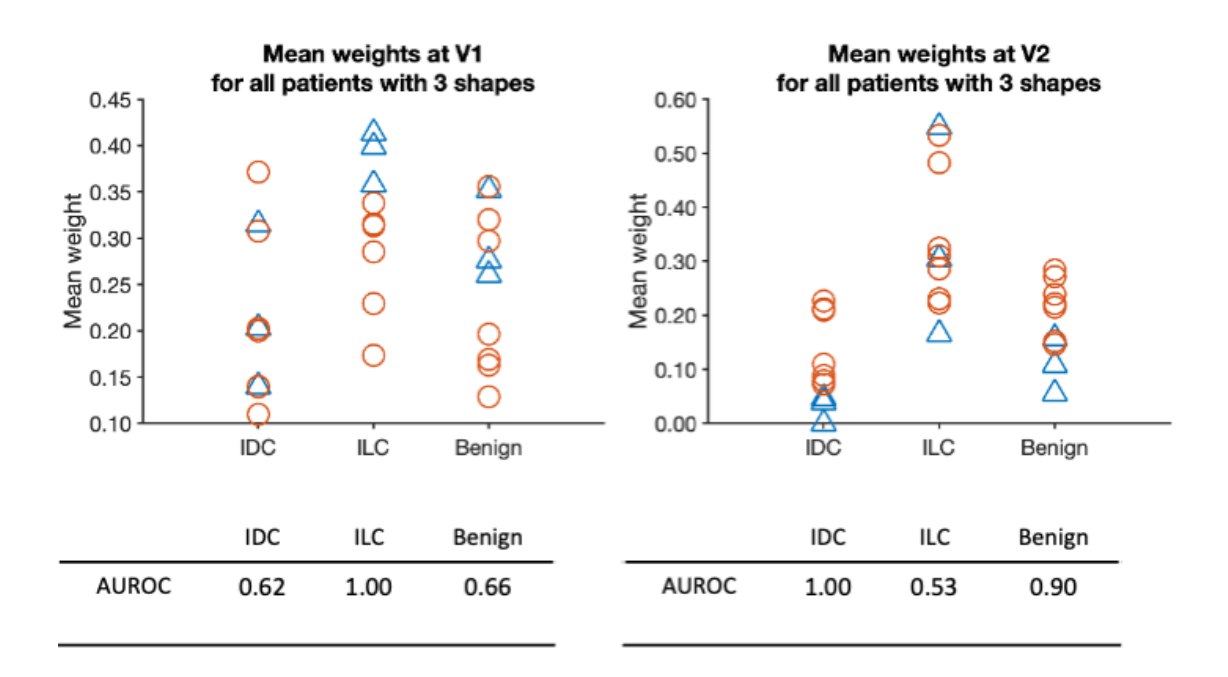


Figure 4-1: Shape analysis with 3 shapes reflecting different types of breast cancer. The mean weights of non-zero voxels for each shape are plotted for each patient at visit 1 (left) and visit 2 (right). The AUROC curve for each shape and visit is plotted below each figure. Each patient's response to neo-adjuvant chemotherapy is labelled as pCR (blue) or non-pCR (orange). Separation of pCR and non-pCR patients occurs in the mean weights for the IDC shape in visit 1 and in the mean weights of the ILC shape for visit 2. This is reflected in AUROC values of 1.

Conducting the analysis with two shapes generated with k_{ep} from the Eliat study (74) and the population average AIF as a third shape did not change the separation between of pCR and non-pCR observed in 2 shape analysis. The AIF term was characterized by small weights in most

voxels, and the meanNZ weights did not show any separation of pCR and non-PCR patients. This is shown in Figure 4-2. The 2-shape analysis in Chapter 3 had mean R² values of 0.81 and 0.70 for visit 1 and visit 2 respectively, while the 2-shape analysis with an AIF term had R² values of 0.81 and 0.71 for visit 1 and visit 2 respectively.

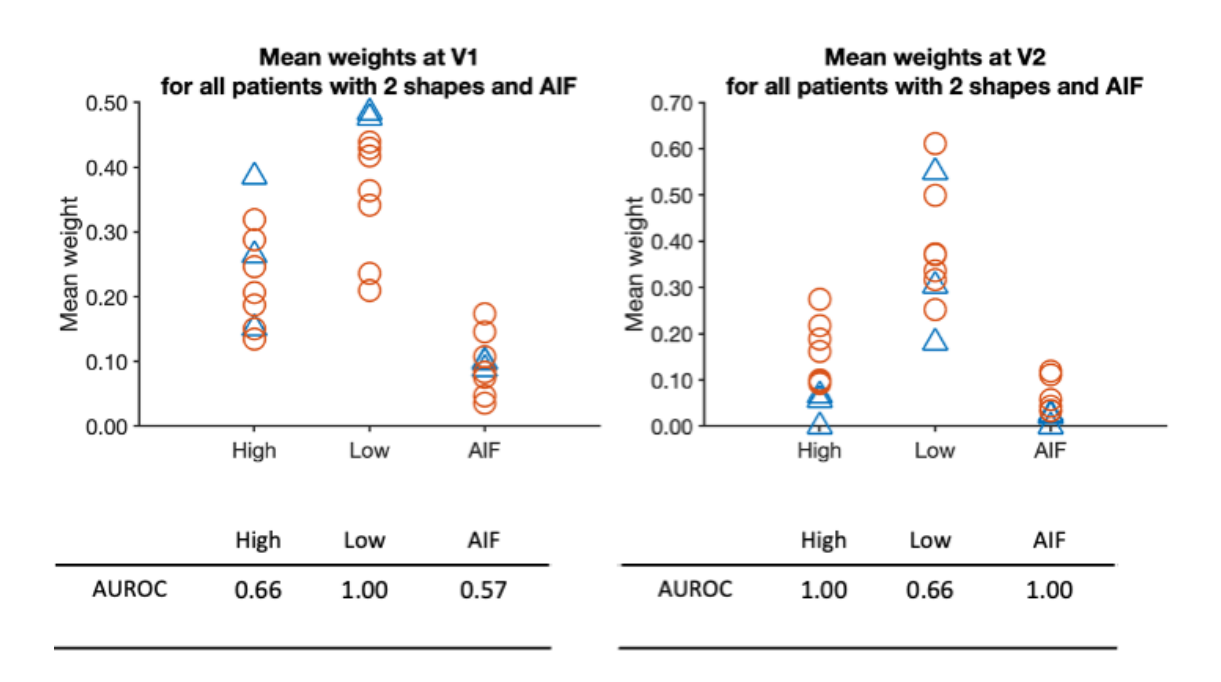


Figure 4-2: Shape analysis with the AIF as a third shape. The mean weights of non-zero voxels for each shape are plotted for each patient at visit 1 (left) and visit 2 (right). Each patient's therapy response is labelled as pCR (blue) or non-pCR (orange). The AUROC curve for each shape and visit is plotted bellow each figure. Separation of pCR and non-pCR patients occurs in the mean weights of high-perfusion shapes for visit 2, and the mean weights for low-perfusion shapes in visit 1. This is reflected in AUROC values of 1. The AIF term was characterized by small weights and appears to separate responders from non-responders at visit 2.

4.1.4 Discussion

Conducting shape analysis with 3 shapes representative of breast tumour subtypes yielded interesting results. The low perfusion shape (k_{ep} =0.32 min⁻¹) previously used in Chapter 3 no

longer showed the response separation at visit 1 and instead the separation was present in the weights of the shape with an intermediate k_{ep} =0.66 min⁻¹. This suggest that the range of k_{ep} values used to define shapes might be more flexible than initially proposed in Chapter 3.

The question of whether our analysis might be instead identifying tumour subtype, which in turn is related to response to chemotherapy, is impossible to assess in a dataset where tumour subtypes were unavailable. If the weights of the shapes were indicative of the tumour subtype, the results would suggest that high ILC and low IDC weights might be associated with a positive response to chemotherapy. The responders at visit 1 had more ILC weight, and the responders at visit 2 had less IDC weights. However, the opposite is reported in literature: ILC has a lower chance of pCR than IDC when treated with neoadjuvant chemotherapy (89). It is therefore unlikely that that our shape recognition method is capturing histological subtype, and that instead we are observing meaningful mixtures of k_{ep} values within voxels.

In addition to running the analysis with 3 shapes, 2 shape analysis was done using the AIF as the third shape. Including an AIF shape in the analysis did not change the separation or the quality of fit meaningfully. In fact, the AIF shape had low mean weights in both visits, not being assigned as part of the model in most voxels.

4.2 Semi-Automatic Region of Interest Generation

4.2.1 Introduction

The dataset used for this study included regions of interest (ROIs) of the breast cancer tumours delineated by an expert. Not all available datasets have ROIs, and this is a major obstacle in applying the proposed analysis to those datasets. Manual contouring is time consuming and is likely to be an operator dependent process. The need for an expert to manually contour the tumours is also a barrier to the proposed analysis in prospective studies and deployment in the clinic.

The objective of the work presented in this section is to propose a semi-automatic technique for contouring the tumour, where the only manual input is a quick and rough contour around the tumour.

4.2.2 Methods

The semi-automatic contours were generated by first drawing a rough mask over the tumour at every slice. The rough mask contained the entire area of rapid enhancement, and a generous amount of surrounding tissue to ensure that the whole lesion was captured. Shape analysis using Eliat *et al.* k_{ep} values (78) was then conducted on the voxels within the rough mask, and the goodness-of-fit was evaluated at each voxel as described in Chapter 3. The voxels were only included in the meanNZ calculation if their R² of the model fit to the data is over 0.5. The threshold of 0.5 was chosen as that is the R² threshold where the model explains 50% of the variance. The semi-automatic contours were compared to the manual contours provided with the data set by calculating the DICE coefficient (90) between the two masks. This process can be seen in Figure 4-3.

This method's ability to reproduce the relationship between therapy response and the weight of shapes was compared with the manual ROIs, and a commonly used simpler ROI method based on a threshold of enhancement. This threshold ROI method begins by first drawing a rough mask over the tumour at every slice. The rough mask contained the entire area of rapid enhancement, and a generous amount of surrounding tissue to ensure that the whole lesion was captured. Relative enhancement was the given by:

$$Relative \ Signal \ Enhancement = \frac{\overline{S_{post}} + \overline{S_{pre}}}{\overline{S_{post}}}$$

(4-1)

Where $\overline{S_{post}}$ is the average signal over all timepoints after the contrast agent is administered and $\overline{S_{pre}}$ is the average signal over all timepoints before the contrast agent is administered. The voxels were only included in the meanNZ calculation if relative threshold enhancement is greater than a chosen threshold.

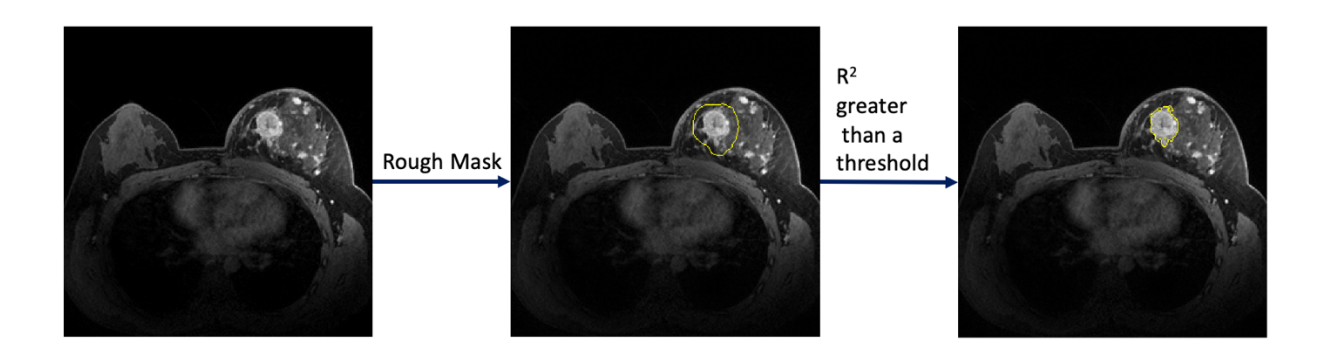


Figure 4-3: Pipeline for semiautomated region of interest. A rough contour (yellow) is drawn around the tumour, followed by two component shape analysis. Then the shape analysis is restricted voxels that had an R^2 value above 0.5. The last image shows the final contour o the semiautomatic ROI (yellow).

4.2.3 Results

The semi-automatic tumour masks seemed to conform to the tumour very well. This was reflected by high DICE coefficients between the manual and semi-automatic masks. Interestingly, every automatic tumour mask was slightly smaller than the manual masks provided with the published dataset. Both these observations are shown Figure 4-4. When looking at the mean weights generated with the semi-automatic ROIs, the same separation of pCR and non-pCR is reproduced in the automatic masks as in the manual masks (reported in Chapter 3). The mean weight is the semi-automatic masks and the same analysis originally reported in Chapter 3 are shown in Figure 4-4. The separation was not present using masks based on a simpler thresholding

technique. Using a mask generated based on a threshold of a percent of the maximum enhancement led to at best only separation of pCR and non-PCR patients based on the mean weights of the high perfusion shapes at visit 2. An example of a 70% threshold is shown in Figure 4-6, but no threshold value was able to reproduce the separation at visit 1 seen in the manual and goodness-of-fit based masks.

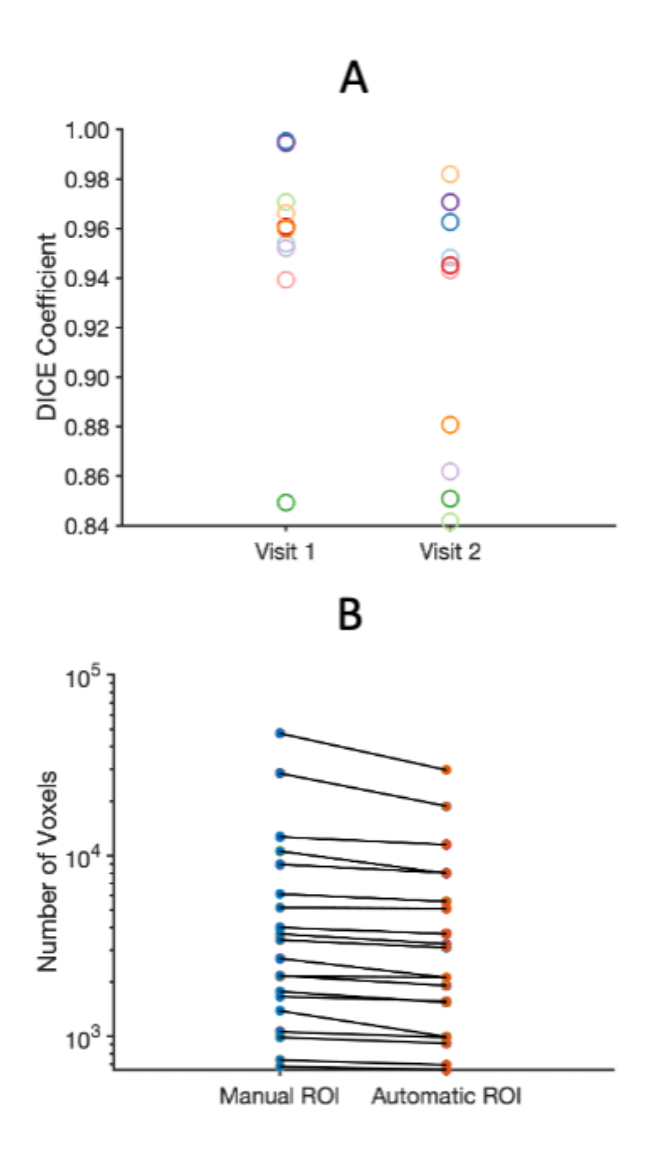


Figure 4-4 The DICE coefficients between the manual contours and the semi-automatic contours based on goodness-of-fit is shown in sub plot A. Patients are separated by visit, and each tumour is plotted by a unique colour that is maintained between visits. The size of the manual and semi-automatic tumour contours is plotted in subplot B. Manual and semi-automatic contours sizes for the same tumours are connected by a black line. The DICE coefficients are high, reflecting good conformity between manual and semi-automatic masks. All semi-automatic masks are smaller than their manually drawn counterparts.

based on Goodness of Fit Mean weights at V1 Mean weights at V2 for all patients for all patients 0.50 0.70 0.60 0.40 0.50 Weg 0.40 0.30 0.20 0.50 Mean weight 0.30 0 0.20 0.20 0 0.10 A High 0.10 0.00 Low High Low **Manual Contouring** Mean weights at V1 Mean weights at V2 for all patients for all patients 0.50 0.70 0.60 8 0.40 Mean weight Mean weight 0.50 0.40 0.30 0.20 0.50 0 0.20 0.20 0 0.10

Semi Automatic Contouring

Figure 4-5: Mean weights with semi-automatic (top) ROI and manual (bottom) contoured tumours. The mean weights of non-zero voxels for each shape are plotted for each patient at visit 1 (left) and visit 2 (right). Each patient's therapy response is labelled as pCR (blue) or non-pCR (orange). Separation of pCR and non-pCR patients occurs in the mean weights for low-perfusion shapes in visit 1 and in the mean weights of high-perfusion shapes for visit 2 for both of the contouring techniques. The mean weights are similar to those seen with manual ROI, and the separation of therapy response is still present.

0.00

Low

High

0.10

Low

High

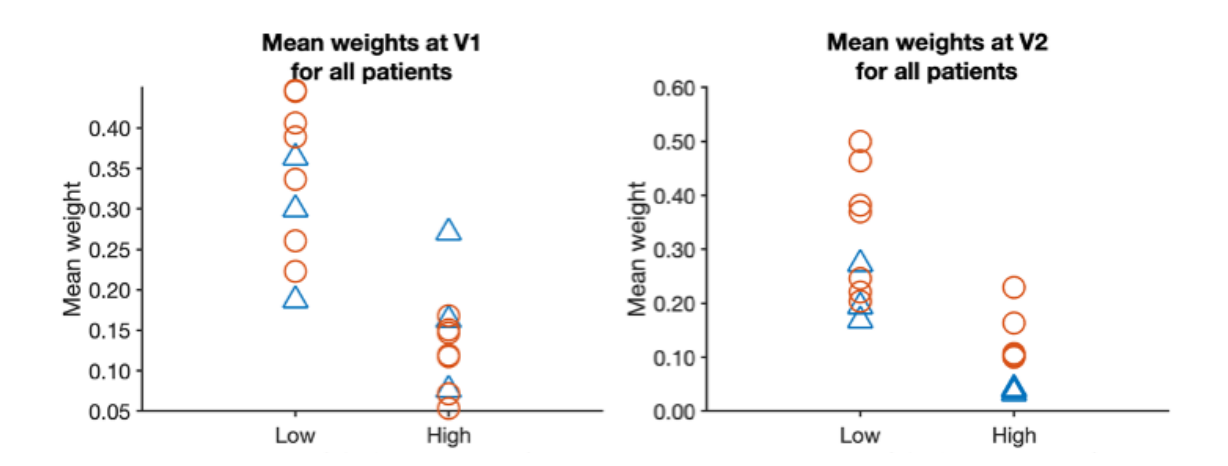


Figure 4-6: Mean weights with semi-automatic threshold ROI. The threshold used was 70% of the maximum enhancement. The mean weights of non-zero voxels for each shape are plotted for each patient at visit 1 (left) and visit 2 (right). Each patient's therapy response is labelled as pCR (blue) or non-pCR (orange). Separation of pCR and non-pCR patients occurs only in the mean weights of high-perfusion shapes for visit 2.

4.2.4 Discussion

To address the obstacle of defining ROIs in datasets without them, a method of semi-automatically generating the ROIs was investigated. The semi-automatic delineation based on goodness-of-fit was able to not only create masks that agreed with the expert contouring of the tumour but was also able to reproduce the treatment response relation using the set of manual ROIs. Simpler methods used to generate ROIs were not able to reproduce this result as shown in Figure 4-6. Interestingly every automatic mask appeared to have fewer voxels and always a subset of the manual mask. One limitation is the fact that this automatic tumour delineation is discarding voxels that the model does not explain, by thresholding to select only voxels with a high coefficient of determination. This design choice should be validated in other datasets.

Chapter 5: Discussion & Conclusion

5.1 Discussion

In Chapter 3 we showed a two-component shape analysis method of analysing breast DCE-MRI data based on shapes defined using the Tofts-Kety model. This method was able to separate patients with breast cancer as complete responders and non-responders to neoadjuvant chemotherapy in a publicly available dataset. This method is fast, with a processing time of a few minutes for 10 patients, and robust to variations or errors in the acquisition. Shape analysis was run with several k_{ep} values defining the shapes, and all selected shapes resulted in the same relationship between therapeutic response and mean weights. An insensitivity to lower temporal resolutions makes this method suitable to apply to clinical data. This method may be a useful tool in predicting therapy response in breast cancers as early as the pre-treatment scan and could be an aid to decisions made by doctors.

One barrier to this method and any quantitative DCE-MRI analysis is the requirement of accurate ROIs delineating the lesions. Contouring of ROIs is usually done manually by an expert but is a time-consuming process. Chapter 4 showed that commonly used algorithms to generate ROIs, such as an approach based on a simple threshold of maximum enhancement, failed to capture enough voxels to reproduce the separation we saw with the manual ROIs in this data set. We proposed and implemented a semi-automatic ROI algorithm based on a threshold of R² values of the goodness-of-fit of shape analysis coupled with a rough manual delineation. This created masks with high conformity to the original manual masks, reflected by a high Dice coefficient. Additionally, these masks captured the relationship seen with the manual masks between the mean weights of the shapes and the eventual therapeutic response. This method is faster than manual contouring with comparable results.

Shape based classification has already seen success in other tissues (27). Our group has tested a version of this approach in liver, which has shown promising preliminary results in identifying cellular growth patterns in colorectal cancer hepatic metastases (unpublished result). DCE is also of interest in soft tissue tumors, where we might obtain grading information. There is evidence for a connection between DCE-MRI quantitative observations of K^{Trans} and k_{ep} and already established histological analysis of microvessel density and percentage of Ki-67 antigen positive cells (91). Another potential application of this analysis is the differentiation of pseudo-progression vs true progression in cerebral metastasis, which showed promise using DCE MRI quantitative parameters such as K^{Trans} (92).

5.2 Future Work

One immediate area of improvement on this study is the application to other datasets. Previously, a constraint was that come candidate datasets did not have ROIs supplied. A ROI generation method based on simple enhancement-based thresholding that we tried was not successful at replicating the results of shape analysis with manual ROIs in the original dataset. Now, with the semi-automated ROI algorithm proposed in Chapter 3, application of shape analysis to these other data sets is possible. This ROI generation method itself can benefit from additional work. The design choice of discarding data that is not explained by the model (described in section 4.2) should be validated in other data sets.

To test the robustness to a lack of a high quality measured AIF, a literature AIF by Parker et al. (44) was used, with mixed results Chapter 3. There are other AIFs available that were not investigated, including the Georgiou AIF (47). Since the publication of the Parker AIF in 2006, DCE-MRI acquisitions have improved in quality, and Georgiou et al. took advantage of this to

publish a functional form of an AIF that better captures the successive passes of the contrast agent bolus that are averaged out in the Parker and averaged AIFs.

Finally, several values of k_{ep} have been reported in literature for benign, malignant, or other subtypes of breast cancers (71, 78-80). k_{ep} values from these studies were all used in shape analysis (in Chapter 4) with all producing the separation between pCR and non-pCR based on the mean weights of shapes. Although the reported k_{ep} values for malignant diseases among all of these studies differed slightly, the reported k_{ep} values for benign lesions was stable around 0.3 min⁻¹. However, as reported in a Chapter 4 using 3 shapes revealed that the value for the low k_{ep} can be much higher (0.66 min⁻¹) and maintain the separation. This opens the question of what range of values of k_{ep} for either high or low shapes is sufficient to retain the separation between responders and non-responders, or to ensure separation on future datasets.

Another limitation of this work is that the analysis focused on the main enhancing region or the tumour, while there were other smaller enhancing "bright spots" in the scan in the surrounding tissue that were not included in the expert's manual contour. It would be interesting to see the weights of shapes assigned to these spots and the quality of the fit.

5.3 Conclusion

A method was presented in this thesis for shape analysis of DCE-MRI that exploits model-based shapes and can separate patients based on eventual response to chemotherapy at least as early as after one cycle of chemotherapy. Simulations and clinical data showed that this method is fast and robust to inaccuracies in acquisition parameters. Along with this, a semi-automatic approach for delineating regions of interest around rapidly enhancing lesions based on the goodness-of-fit of the shape analysis method was also presented. Going forward, this method is

promising as an alternative to quantitative model-based analysis of DCE-MRI that retains information from a physical description of the enhancement dynamics.

REFERENCES

- 1. Mann RM, Cho N, Moy L. Breast MRI: State of the art. Radiology. 2019;292(3):520-36.
- 2. Yankeelov TE, Gore JC. Dynamic contrast enhanced magnetic resonance imaging in oncology: theory, data acquisition, analysis, and examples. Current Medical Imaging. 2007;3(2):91-107.
- 3. Lavini C, Buiter MS, Maas M. Use of dynamic contrast enhanced time intensity curve shape analysis in MRI: Theory and practice. Reports in Medical Imaging 2013. p. 71-82.
- 4. Kuhl CK, Mielcareck P, Klaschik S, Leutner C, Wardelmann E, Gieseke J, et al. Dynamic breast MR imaging: are signal intensity time course data useful for differential diagnosis of enhancing lesions? Radiology. 1999;211(1):101-10.
- 5. Rijswijk CSPv, Geirnaerdt MJA, Hogendoorn PCW, Taminiau AHM, Coevorden Fv, Zwinderman AH, et al. Soft-Tissue Tumors: Value of Static and Dynamic Gadopentetate Dimeglumine—enhanced MR Imaging in Prediction of Malignancy. Radiology. 2004;233(2):493-502.
- 6. Flickinger FW, Allison JD, Sherry RM, Wright JC. Differentiation of benign from malignant breast masses by time-intensity evaluation of contrast enhanced MRI. Magnetic Resonance Imaging. 1993;11(5):617-20.
- 7. Nagel E, Klein C, Paetsch I, Hettwer S, Schnackenburg B, Wegscheider K, et al. Magnetic resonance perfusion measurements for the noninvasive detection of coronary artery disease. Circulation. 2003;108(4):432-7.
- 8. Evelhoch JL. Key factors in the acquisition of contrast kinetic data for oncology. Journal of Magnetic Resonance Imaging. 1999;10(3):254-9.
- 9. Hauth EA, Stockamp C, Maderwald S, Mühler A, Kimmig R, Jaeger H, et al. Evaluation of the three-time-point method for diagnosis of breast lesions in contrast-enhanced MR mammography. Clinical imaging. 2006;30(3):160-5.
- 10. Lauffer RB. Paramagnetic metal complexes as water proton relaxation agents for NMR imaging: theory and design. Chemical reviews. 1987;87(5):901-27.
- 11. Tofts PS, Brix G, Buckley DL, Evelhoch JL, Henderson E, Knopp MV, et al. Estimating Kinetic Parameters From Dynamic Contrast-Enhanced T 1-Weighted MRI of a Diffusable Tracer: Standardized Quantities and Symbols. 1999.
- 12. Larsson H, Stubgaard M, Frederiksen J, Jensen M, Henriksen O, Paulson O. Quantitation of blood-brain barrier defect by magnetic resonance imaging and gadolinium-DTPA in patients with multiple sclerosis and brain tumors. Magnetic Resonance in Medicine. 1990;16(1):117-31.
- 13. Brix G, Semmler W, Port R, Schad LR, Layer G, Lorenz WJ. Pharmacokinetic parameters in CNS Gd-DTPA enhanced MR imaging. Journal of computer assisted tomography. 1991;15(4):621-8.
- 14. Patlak CS, Blasberg RG, Fenstermacher JD. Graphical evaluation of blood-to-brain transfer constants from multiple-time uptake data. Journal of Cerebral Blood Flow & Metabolism. 1983;3(1):1-7.
- 15. Sourbron S, Ingrisch M, Siefert A, Reiser M, Herrmann K. Quantification of cerebral blood flow, cerebral blood volume, and blood—brain-barrier leakage with DCE-MRI. Magnetic Resonance in Medicine: An Official Journal of the International Society for Magnetic Resonance in Medicine. 2009;62(1):205-17.
- 16. Tofts PS. T1-weighted DCE imaging concepts: modelling, acquisition and analysis. signal. 2010;500(450):400.
- 17. Bushberg JT, Boone JM. The essential physics of medical imaging: Lippincott Williams & Wilkins; 2011.
- 18. Nishimura DG. Principles of magnetic resonance imaging: Standford Univ.; 2010.
- 19. Bley TA, Wieben O, François CJ, Brittain JH, Reeder SB. Fat and water magnetic resonance imaging. Journal of Magnetic Resonance Imaging. 2010;31(1):4-18.
- 20. Huang W, Li X, Chen Y, Li X, Chang MC, Oborski MJ, et al. Variations of dynamic contrast-enhanced magnetic resonance imaging in evaluation of breast cancer therapy response: A multicenter data analysis challenge. Translational Oncology. 2014;7(1):153-66.

- 21. Chang LC, Koay CG, Basser PJ, Pierpaoli C. Linear least-squares method for unbiased estimation of T1 from SPGR signals. Magnetic Resonance in Medicine: An Official Journal of the International Society for Magnetic Resonance in Medicine. 2008;60(2):496-501.
- 22. Cheng HLM, Wright GA. Rapid high-resolution T1 mapping by variable flip angles: accurate and precise measurements in the presence of radiofrequency field inhomogeneity. Magnetic Resonance in Medicine: An Official Journal of the International Society for Magnetic Resonance in Medicine. 2006;55(3):566-74.
- 23. Partridge SC, Stone KM, Strigel RM, DeMartini WB, Peacock S, Lehman CD. Breast DCE-MRI: influence of postcontrast timing on automated lesion kinetics assessments and discrimination of benign and malignant lesions. Academic radiology. 2014;21(9):1195-203.
- 24. Khalifa F, Soliman A, El-Baz A, Abou El-Ghar M, El-Diasty T, Gimel'farb G, et al. Models and methods for analyzing DCE-MRI: A review. Medical physics. 2014;41(12):124301.
- 25. Breast M. State of the Art. Ritse M. Mann, Nariya Cho, Linda Moy. Radiology. 2019;292:520-36.
- 26. Degani H, Gusis V, Weinstein D, Fields S, Strano S. Mapping pathophysiological features of breast tumors by MRI at high spatial resolution. Nature medicine. 1997;3(7):780-2.
- 27. Lavini C, de Jonge MC, van de Sande MGH, Tak PP, Nederveen AJ, Maas M. Pixel-by-pixel analysis of DCE MRI curve patterns and an illustration of its application to the imaging of the musculoskeletal system. Magnetic Resonance Imaging. 2007;25(5):604-12.
- 28. Sung JS, Stamler S, Brooks J, Kaplan J, Huang T, Dershaw DD, et al. Breast cancers detected at screening MR imaging and mammography in patients at high risk: method of detection reflects tumor histopathologic results. Radiology. 2016;280(3):716.
- 29. Tofts PS, Kermode AG. Measurement of the blood-brain barrier permeability and leakage space using dynamic MR imaging. 1. Fundamental concepts. Magnetic resonance in medicine. 1991;17(2):357-67.
- 30. Jackson A, Li KL, Zhu X. Semi-quantitative parameter analysis of DCE-MRI revisited: Monte-Carlo simulation, clinical comparisons, and clinical validation of measurement errors in patients with type 2 neurofibromatosis. PLoS ONE. 2014;9(3).
- 31. Ramalho J, Semelka R, Ramalho M, Nunes R, AlObaidy M, Castillo M. Gadolinium-based contrast agent accumulation and toxicity: an update. American Journal of Neuroradiology. 2016;37(7):1192-8.
- 32. Kety SS. The theory and application of the exchange of inert gas at the lungs and tissues. Pharmacol rev. 1951;3:1-41.
- 33. Tofts PS, Brix G, Buckley DL, Evelhoch JL, Henderson E, Knopp MV, et al. Estimating kinetic parameters from dynamic contrast-enhanced T1-weighted MRI of a diffusable tracer: standardized quantities and symbols. Journal of Magnetic Resonance Imaging: An Official Journal of the International Society for Magnetic Resonance in Medicine. 1999;10(3):223-32.
- 34. Sourbron SP, Buckley DL. On the scope and interpretation of the Tofts models for DCE-MRI. Magnetic Resonance in Medicine. 2011;66(3):735-45.
- 35. Henderson E, Rutt BK, Lee T-Y. Temporal sampling requirements for the tracer kinetics modeling of breast disease. Magnetic resonance imaging. 1998;16(9):1057-73.
- 36. Larsson C, Kleppestø M, Rasmussen Jr I, Salo R, Vardal J, Brandal P, et al. Sampling requirements in DCE-MRI based analysis of high grade gliomas: simulations and clinical results. Journal of Magnetic Resonance Imaging. 2013;37(4):818-29.
- 37. Cuenod CA, Balvay D. Perfusion and vascular permeability: Basic concepts and measurement in DCE-CT and DCE-MRI. Diagnostic and Interventional Imaging: Elsevier Masson SAS; 2013. p. 1187-204.
- 38. Wang H, Cao Y. Correction of arterial input function in dynamic contrast-enhanced MRI of the liver. Journal of Magnetic Resonance Imaging. 2012;36(2):411-21.
- 39. Roberts C, Little R, Watson Y, Zhao S, Buckley DL, Parker GJ. The effect of blood inflow and B1-field inhomogeneity on measurement of the arterial input function in axial 3D spoiled gradient echo dynamic contrast-enhanced MRI. Magnetic resonance in medicine. 2011;65(1):108-19.

- 40. Koestler H, Ritter C, Lipp M, Beer M, Hahn D, Sandstede J. Prebolus quantitative MR heart perfusion imaging. Magnetic Resonance in Medicine: An Official Journal of the International Society for Magnetic Resonance in Medicine. 2004;52(2):296-9.
- 41. Garpebring A, Wirestam R, Östlund N, Karlsson M. Effects of inflow and radiofrequency spoiling on the arterial input function in dynamic contrast-enhanced MRI: a combined phantom and simulation study. Magnetic Resonance in Medicine. 2011;65(6):1670-9.
- 42. Kotys MS, Akbudak E, Markham J, Conturo TE. Precision, signal-to-noise ratio, and dose optimization of magnitude and phase arterial input functions in dynamic susceptibility contrast MRI. Journal of Magnetic Resonance Imaging: An Official Journal of the International Society for Magnetic Resonance in Medicine. 2007;25(3):598-611.
- 43. Kovar DA, Lewis M, Karczmar GS. A new method for imaging perfusion and contrast extraction fraction: input functions derived from reference tissues. Journal of Magnetic Resonance Imaging. 1998;8(5):1126-34.
- 44. Parker GJ, Roberts C, Macdonald A, Buonaccorsi GA, Cheung S, Buckley DL, et al. Experimentally-derived functional form for a population-averaged high-temporal-resolution arterial input function for dynamic contrast-enhanced MRI. Magnetic Resonance in Medicine: An Official Journal of the International Society for Magnetic Resonance in Medicine. 2006;56(5):993-1000.
- 45. Whitcher B, Schmid VJ. Quantitative analysis of dynamic contrast-enhanced and diffusion-weighted magnetic resonance imaging for oncology in R. Journal of Statistical Software. 2011;44:1-29.
- 46. Fritz-Hansen T, Rostrup E, Larsson HB, Søndergaard L, Ring P, Henriksen O. Measurement of the arterial concentration of Gd-DTPA using MRI: a step toward quantitative perfusion imaging. Magnetic Resonance in Medicine. 1996;36(2):225-31.
- 47. Georgiou L, Wilson DJ, Sharma N, Perren TJ, Buckley DL. A functional form for a representative individual arterial input function measured from a population using high temporal resolution DCE MRI. Magnetic Resonance in Medicine. 2019;81(3):1955-63.
- 48. Shukla-Dave A, Lee N, Stambuk H, Wang Y, Huang W, Thaler HT, et al. Average arterial input function for quantitative dynamic contrast enhanced magnetic resonance imaging of neck nodal metastases. BMC medical physics. 2009;9(1):1-9.
- 49. Ah-See M-LW, Makris A, Taylor NJ, Harrison M, Richman PI, Burcombe RJ, et al. Early changes in functional dynamic magnetic resonance imaging predict for pathologic response to neoadjuvant chemotherapy in primary breast cancer. Clinical Cancer Research. 2008;14(20):6580-9.
- 50. Johansen R, Jensen LR, Rydland J, Goa PE, Kvistad KA, Bathen TF, et al. Predicting survival and early clinical response to primary chemotherapy for patients with locally advanced breast cancer using DCE-MRI. Journal of Magnetic Resonance Imaging: An Official Journal of the International Society for Magnetic Resonance in Medicine. 2009;29(6):1300-7.
- 51. Martincich L, Montemurro F, Cirillo S, Marra V, De Rosa G, Ponzone R, et al. Role of Magnetic Resonance Imaging in the prediction of tumor response in patients with locally advanced breast cancer receiving neoadjuvant chemo-therapy. La Radiologia Medica. 2003;106(1-2):51-8.
- 52. Chen F-H, Wang C-C, Liu H-L, Fu S-Y, Yu C-F, Chang C, et al. Decline of tumor vascular function as assessed by dynamic Contrast-Enhanced magnetic resonance imaging is associated with poor responses to radiation therapy and chemotherapy. International Journal of Radiation Oncology* Biology* Physics. 2016;95(5):1495-503.
- 53. Yu HJ, Chen JH, Mehta RS, Nalcioglu O, Su MY. MRI measurements of tumor size and pharmacokinetic parameters as early predictors of response in breast cancer patients undergoing neoadjuvant anthracycline chemotherapy. Journal of Magnetic Resonance Imaging. 2007;26(3):615-23.
- 54. Carol D, Rebecca S, Priti B, Ahmedin J. Breast cancer statistics, 2013. CA Cancer J Clin. 2014;64(1):52-62.
- 55. Richie RC, Swanson JO. Breast cancer: a review of the literature. JOURNAL OF INSURANCE MEDICINE-NEW YORK THEN DENVER--. 2003;35(2):85-101.

- 56. Menezes GLG, Knuttel FM, Stehouwer BL, Pijnappel RM, Van Den Bosch MAAJ. Magnetic resonance imaging in breast cancer: A literature review and future perspectives. World Journal of Clinical Oncology: Baishideng Publishing Group Co., Limited; 2014. p. 61-70.
- 57. Selvi V, Nori J, Meattini I, Francolini G, Morelli N, Di Benedetto D, et al. Role of magnetic resonance imaging in the preoperative staging and work-up of patients affected by invasive lobular carcinoma or invasive ductolobular carcinoma. BioMed research international. 2018;2018.
- 58. Biglia N, Mariani L, Sgro L, Mininanni P, Moggio G, Sismondi P. Increased incidence of lobular breast cancer in women treated with hormone replacement therapy: implications for diagnosis, surgical and medical treatment. Endocrine-related cancer. 2007;14(3):549-67.
- 59. Warner E, Messersmith H, Causer P, Eisen A, Shumak R, Plewes D. Systematic review: using magnetic resonance imaging to screen women at high risk for breast cancer. Annals of internal medicine. 2008;148(9):671-9.
- 60. Sardanelli F, Boetes C, Borisch B, Decker T, Federico M, Gilbert FJ, et al. Magnetic resonance imaging of the breast: recommendations from the EUSOMA working group. European journal of cancer. 2010;46(8):1296-316.
- 61. Yoo EY, Nam SY, Choi H-Y, Hong MJ. Agreement between MRI and pathologic analyses for determination of tumor size and correlation with immunohistochemical factors of invasive breast carcinoma. Acta radiologica. 2018;59(1):50-7.
- 62. Partridge SC, McDonald ES. Diffusion weighted magnetic resonance imaging of the breast: protocol optimization, interpretation, and clinical applications. Magnetic Resonance Imaging Clinics. 2013;21(3):601-24.
- 63. Dorrius MD, Dijkstra H, Oudkerk M, Sijens PE. Effect of b value and pre-admission of contrast on diagnostic accuracy of 1.5-T breast DWI: a systematic review and meta-analysis. European radiology. 2014;24(11):2835-47.
- 64. Pediconi F, Catalano C, Padula S, Roselli A, Dominelli V, Cagioli S, et al. Contrast-enhanced MR mammography: improved lesion detection and differentiation with gadobenate dimeglumine. American Journal of Roentgenology. 2008;191(5):1339-46.
- 65. Carbonaro LA, Pediconi F, Verardi N, Trimboli RM, Calabrese M, Sardanelli F. Breast MRI using a high-relaxivity contrast agent: an overview. American journal of roentgenology. 2011;196(4):942-55.
- 66. Flanagan F, Murray J, Gilligan P, Stack J, Ennis J. Digital subtraction in Gd-DTPA enhanced imaging of the breast. Clinical radiology. 1995;50(12):848-54.
- 67. Cheung HS, Gary MT, Lai S-Y, Yeung DK. Relationship between lesion size and signal enhancement on subtraction fat-suppressed MR imaging of the breast. Magnetic resonance imaging. 2004;22(9):1259-64.
- 68. Mann RM, Kuhl CK, Kinkel K, Boetes C. Breast MRI: Guidelines from the European Society of Breast Imaging. European Radiology. 2008;18(7):1307-18.
- 69. Mus RD, Borelli C, Bult P, Weiland E, Karssemeijer N, Barentsz JO, et al. Time to enhancement derived from ultrafast breast MRI as a novel parameter to discriminate benign from malignant breast lesions. European journal of radiology. 2017;89:90-6.
- 70. Onishi N, Kataoka M, Kanao S, Sagawa H, Iima M, Nickel MD, et al. Ultrafast dynamic contrast-enhanced mri of the breast using compressed sensing: breast cancer diagnosis based on separate visualization of breast arteries and veins. Journal of Magnetic Resonance Imaging. 2018;47(1):97-104.
- 71. Tofts PS. Modeling tracer kinetics in dynamic Gd-DTPA MR imaging. Journal of magnetic resonance imaging. 1997;7(1):91-101.
- 72. Leach M, Morgan B, Tofts P, Buckley D, Huang W, Horsfield M, et al. Experimental Cancer Medicine Centres Imaging Network Steering C (2012) Imaging vascular function for early stage clinical trials using dynamic contrast-enhanced magnetic resonance imaging. Eur Radiol.22(7):1451-64.
- 73. Huang B, Wong C-S, Whitcher B, Kwong DL-W, Lai V, Chan Q, et al. Dynamic contrast-enhanced magnetic resonance imaging for characterising nasopharyngeal carcinoma: comparison of

- semiquantitative and quantitative parameters and correlation with tumour stage. European radiology. 2013;23(6):1495-502.
- 74. Beuzit L, Eliat PA, Brun V, Ferré JC, Gandon Y, Bannier E, et al. Dynamic contrast-enhanced MRI: Study of inter-software accuracy and reproducibility using simulated and clinical data. Journal of magnetic resonance imaging. 2016;43(6):1288-300.
- 75. Tofts PS, Berkowitz B, Schnall MD. Quantitative Analysis of Dynamic Gd-DTPA Enhancement in Breast Tumors Using a Permeability Model. Magnetic Resonance in Medicine. 1995;33(4):564-8.
- 76. Huang W, Li X, Chen Y, Li X, Chang M-C, Oborski MJ, et al. Variations of dynamic contrastenhanced magnetic resonance imaging in evaluation of breast cancer therapy response: a multicenter data analysis challenge. Translational oncology. 2014;7(1):153-66.
- 77. Lawson CL, Hanson RJ. Solving least squares problems: SIAM; 1995.
- 78. Eliat P-A, Dedieu V, Bertino C, Bouté V, Lacroix J, Constans J-M, et al. Magnetic resonance imaging contrast-enhanced relaxometry of breast tumors: an MRI multicenter investigation concerning 100 patients. Magnetic resonance imaging. 2004;22(4):475-81.
- 79. Furman-Haran E, Schechtman E, Kelcz F, Kirshenbaum K, Degani H. Magnetic resonance imaging reveals functional diversity of the vasculature in benign and malignant breast lesions. Cancer. 2005;104(4):708-18.
- 80. Vincensini D, Dedieu Vr, Eliat PA, Vincent C, Bailly C, de Certaines J, et al. Magnetic resonance imaging measurements of vascular permeability and extracellular volume fraction of breast tumors by dynamic Gd-DTPA-enhanced relaxometry. Magnetic Resonance Imaging. 2007;25(3):293-302.
- 81. Whittall KP, MacKay AL. Quantitative interpretation of NMR relaxation data. Journal of Magnetic Resonance. 1989;84:134-52.
- 82. Kershaw LE, Cheng HLM. Temporal resolution and SNR requirements for accurate DCE-MRI data analysis using the AATH model. Magnetic Resonance in Medicine. 2010;64(6):1772-80.
- 83. van der Leij C, van de Sande MG, Lavini C, Tak PP, Maas M. Rheumatoid synovial inflammation: pixel-by-pixel dynamic contrast-enhanced MR imaging time-intensity curve shape analysis-A feasibility study. Radiology. 2009;253(1):234.
- 84. Ziech ML, Lavini C, Bipat S, Ponsioen CY, Spijkerboer AM, Stokkers PC, et al. Dynamic contrastenhanced MRI in determining disease activity in perianal fistulizing Crohn disease: a pilot study. American Journal of Roentgenology. 2013;200(2):W170-W7.
- 85. Jahani N, Cohen E, Hsieh MK, Weinstein SP, Pantalone L, Hylton N, et al. Prediction of Treatment Response to Neoadjuvant Chemotherapy for Breast Cancer via Early Changes in Tumor Heterogeneity Captured by DCE-MRI Registration. Scientific Reports. 2019;9(1).
- 86. Li X, Huang W, Morris EA, Tudorica LA, Seshan VE, Rooney WD, et al. Dynamic NMR effects in breast cancer dynamic-contrast-enhanced MRI. Proceedings of the National Academy of Sciences. 2008;105(46):17937-42.
- 87. Li X, Abramson RG, Arlinghaus LR, Kang H, Chakravarthy AB, Abramson VG, et al. Multiparametric magnetic resonance imaging for predicting pathological response after the first cycle of neoadjuvant chemotherapy in breast cancer. Investigative radiology. 2015;50(4):195-204.
- 88. Arpino G, Bardou VJ, Clark GM, Elledge RM. Infiltrating lobular carcinoma of the breast: tumor characteristics and clinical outcome. Breast cancer research. 2004;6(3):1-8.
- 89. Truin WM, Vugts GM, Roumen RMHMDP, Maaskant-Braat AJGMDP, Nieuwenhuijzen GAPMDP, van der Heiden-van der Loo MP, et al. Differences in Response and Surgical Management with Neoadjuvant Chemotherapy in Invasive Lobular Versus Ductal Breast Cancer. Annals of Surgical Oncology. 2016;23(1):51-7.
- 90. Sorensen TA. A method of establishing groups of equal amplitude in plant sociology based on similarity of species content and its application to analyses of the vegetation on Danish commons. Biol Skar. 1948;5:1-34.

- 91. Zhang Y, Zhao H, Liu Y, Zeng M, Zhang J, Hao D. Diagnostic Performance of Dynamic Contrast-Enhanced MRI and 18F-FDG PET/CT for Evaluation of Soft Tissue Tumors and Correlation with Pathology Parameters. Academic Radiology. 2022.
- 92. Knitter JR, Erly WK, Stea BD, Lemole GM, Germano IM, Doshi AH, et al. Interval change in diffusion and perfusion MRI parameters for the assessment of pseudoprogression in cerebral metastases treated with stereotactic radiation. American Journal of Roentgenology. 2018;211(1):168-75.